Automated reconstruction of tree and canopy structure for modeling the internal canopy radiation regime

Van Leeuwen, Martin ✉[1)], Coops, Nicholas C.[1)], Hilker, Thomas[2, 3)], Wulder, Michael A.[4)], Newnham, Glenn J.[5)], Culvenor, Darius S.[5)]

✉ Corresponding author

1) Forest Resources Management, University of British Columbia, 2424 Main Mall, Vancouver, V6T 1Z4, BC, Canada
2) NASA Goddard Space Flight Centre, Biospheric Sciences Branch Code 618, Bld 33, #G310, 8800 Greenbelt Road, Greenbelt, MD 20771, USA
3) College of Forestry, Oregon State University, 231 Peavy Hall, Corvallis, OR 97331, USA
4) Canadian Forest Service, Natural Resources Canada, 506 West Burnside Road, Victoria, British Columbia, V8Z 1M5, BC, Canada
5) Commonwealth Scientific and Industrial Research Organisation (CSIRO), Locked Bag 10, Clayton South VIC 3139, Australia

Keywords: Laser scanning, canopy structure, photosynthetically active radiation, explicit geometric, modeling

Pre-print of published version.

Reference:

van Leeuwen, Martin; Coops, Nicholas C.; Hilker, Thomas; Wulder, Michael A.; Newnham, Glenn J.; Culvenor, Darius S. (2013). Automated reconstruction of tree and canopy structure for modeling the internal canopy radiation regime. Remote Sensing of Environment 136: 286–300.

DOI:

http://dx.doi.org/10.1016/j.rse.2013.04.019.

Abstract

Understanding canopy radiation regimes is critical to successfully modeling vegetation growth and function. For instance, the vertical distribution of photosynthetically active radiation (PAR) affects vegetation growth, informative upon carbon and energy cycling. Availing upon advances in information capture and computing power, geometrically explicit modeling of forest structure becomes increasingly possible. A primary challenge however is acquiring the forest mensuration data required to parameterize these models and the related automation of modeling forest structure. In this research, to address these issues we employ a novel and automated approach that capitalizes upon the rich information afforded by ground-based laser scanning technology. The method is implemented in two steps: in the first step, geometric explicit models of canopy structure are created from the ground-based laser scanning data. These geometric explicit models are used to simulate the vertical range to first hit. In the second step, we derive canopy gap probability from full waveform laser scanning data which have been used in a number of studies for characterization of radiation transmission (Yang et al. 2010; Jupp et al. 2009) and does not require any geometric explicit modeling. The radiative consistency of the geometric explicit models from step 1 is validated against the gap probabilities of step 2. The results show a strong relationship between the radiative transmission properties of the geometric models and canopy gap probabilities at plot level (R = 0.91 to 0.97), while the geometric models suggest the additional benefit to serve as a bridge in scaling between shoot level and canopy level radiation.

1. Introduction

Canopy structure encompasses the spatial distribution of foliage as well as the architecture of the supporting woody components such as stems and fine branches. For coniferous canopies, the distribution of foliage elements is typically described around three levels of organization (Oker-Blom 1986): 1) the clumping of needles into shoots, 2) the clumping of shoots around branches, and 3) the clumping of the canopy into crowns. This complex arrangement of foliage elements increases radiation penetration to lower canopy strata (Stenberg 1995; Oker-Blom 1985, 1986) and affects the adaptation of foliage elements to their immediate radiation environment with important implications for forest growth and productivity (Field 1983; Givnish 1988). Over large spatial scales, an exponential decay in radiation with canopy depth is observed. This rate of decay increases with leaf area and decreases with clumping; However, profound deviations from an exponential relation or even abrupt changes (lumiclines) in canopy radiation can be observed over finer spatial scales or along vertical canopy transects (Parker et al. 2001).

Canopy radiation can be computed using radiative transfer models that relate the absorption, reflection, and transmission of radiation to the biophysical characteristics of foliage elements and their spatial arrangement within the canopy. Radiative transfer models range from high spectral resolutions (Jacquemoud et al. 2009) to fine spatially explicit models of canopy structure (Welles and Norman, 1991; Ross and Marshak 1991). These finer levels of geometric detail enable the comparison of simulated radiation budgets against *in situ* measurements (Mariscal et al. 2004), facilitate coupling with leaf or shoot level functional models (Van der Tol, 2009; Wang and Jarvis, 1990), and provide for a benchmark that can be used to evaluate model performances that operate at wider scales (Widlowski et al. 2006). The parameterization of the latter models is challenging and costly, due to the large number of structural parameters.

Ground based laser scanning is a recent technology that has significant potential for direct and cost-efficient measurement of forest structure at very high resolutions. Canopy structure is digitized by emitting laser pulses across a wide field of view and measuring the time of flight between each emission, reflection off any scanned targets, and return at the instrument (Aschoff and Spiecker 2004). The recorded laser returns may be digitized as full waveform data, where the full return of laser energy is recorded at a nanosecond bandwidth, or as discrete returns, where data is represented as point clouds. In forestry, these data have been used for the modeling of stem volume and taper (Maas et al. 2008), branching structures (Bucksch et al., 2010), and - in combination with tree modeling techniques such as L-systems (Prusinkiewicz and Lindemayer, 1990) - the reconstruction of individual trees at levels of detail beyond the shoot scale (Côté et al. 2009, 2011).

The high level of structural detail of these data provides an important opportunity to parameterize geometrically explicit radiative transfer models. Modeling approaches have primarily focused on using point cloud information and generally require various assumptions on growth patterns and foliage characteristics. Methods typically start with the segmentation of returns into woody material and foliage, e.g. based on return intensities (Côté et al. 2009) after which geometries of tree trunks and branching can be obtained. To address effects of data obscuration and roughness of object surfaces (Côté et al. 2011; Liang et al. 2012) least squares optimization (Maas et al. 2008) and hypothesis testing and generating techniques such as Hough transform (Fleck et al. 2004) have been adopted. Coarse topological graphs of branching structures may be created using skeletonization algorithms such as provided by Verroust and Lazarus (2000) and Bucksch et al. (2010). More recent developments in modeling tree structure have combined laser scanner data with tree architectural software to represent levels of detail beyond the shoot. This is achieved by simulating the growth of fine woody structures that follow the spatial distribution of foliage returns or that adapt to simulations of the internal canopy radiation regime (Runions et al. 2007; Côté et al. 2009, 2011; Van der Zande, 2011).

A number of challenges remain in modeling of canopy structure at scales ranging from individual shoots to the crown level. Data obscuration makes the automation of the modeling pipeline challenging (Côté et al. 2011) and the level of detail of crown and canopy reconstructions needs to be balanced with computational tractability while remaining able to simulate canopy radiation profiles.

In this paper we present a methodology for the automated reconstruction of canopy structure from ground-based laser scanning data into three-dimensional mesh models that provide for modeling radiation transmission with canopy depth. The data used in the reconstruction pipeline are discrete but the point clouds are derived from full waveform data. We then compare and evaluate this method of reconstruction against an established method for deriving canopy radiation transmission from the full waveform data and evaluate the radiative consistency between these two approaches. We conclude the paper with a discussion on the use of these modeling techniques and opportunities for analysis of shoot level functioning.

2. Methods

2.1 Study area

The study area is a coastal coniferous forest in the dry maritime Coastal Western Hemlock subzone (Humphreys et al. 2006) on the east coast of Vancouver Island, British Columbia, Canada, approximately 20 km south of Campbell River. The stand chosen consists mainly of Douglas-fir *[Pseudotsuga menziesii var. menziesii (Mirb.) Franco],* and a minority of western red cedar *[Thuja plicata Donn. ex D. Don],* and western hemlock *[Tsuga heterophylla (Raf.) Sarg.]* that comprises 17% and 3% respectively

(Morgenstern et al. 2004). Trees are around 60 years-old, between 30 - 35 m in height with a stand density approximating 1100 stems ha^{-1} (Jassal et al. 2009). The understory is sparse and mainly consists of salal *[Gaultheria shallon Pursh.]*, Oregon grape *[Berberis nervosa Pursh.]*, and vanilla-leaf deer foot *[Achlys triphylla DC]*, with a shallow layer of ferns and mosses. A total of four 30 x 30 m plots are established based on representativeness of the stand of which one (plot 7) was nitrogen enriched (Hilker et al. 2012).

2.2. Data

Field data collected at all four plots included diameter at breast height (DBH), tree height, and stem locations. Stem locations and heights were measured using a vertex (Haglöf, Sweden) hypsometer and compass bearing and DBH was measured using a diameter tape measure. Laser scanning data was acquired using the Echidna™ Validation Instrument (EVI) (Strahler et al. 2008). This laser scanner features a 1064 nm laser light source and digitizes full returned energy at 2 Giga samples per second (Gs/s) and covers a field of view of 360 degrees azimuth and 130 degrees zenith. Data was collected in August 2008 using an angular sampling interval of 4 mrad and beam divergence of 5 mrad and range measurements were cut off if values exceeded 100 m. Five scans per plot were acquired comprising the four plot corners and the centre. North was marked in the scans using a reflective marker that was placed using a compass and coordinates of scan locations were recorded using GPS.

2.3. Data processing

2.3.1. Preprocessing

The full waveform digitization from the EVI instrument is beneficial for analyzing surface scattering where the size of the scatterers is fine compared to the instrument footprint, as this leads to a degree of porosity of the medium to the laser beam that can be used for modeling the transmission of radiation through the canopy (Yang et al. 2010; Jupp et al. 2009). In this study, the full-waveform data was used to derive foliage profiles and canopy gap fraction, the latter is used as a measure of radiation transmission. Single and last returns were used for creating virtual geometric models of the forest plots. These returns were obtained from the full waveform information using methods described by Yang et al. (2013). The single and last returns were projected using the recorded azimuth and zenith angles of the respective laser shots into the 2D image domain (Andrieu et al. 1994). The same projection was then used to produce a suite of additional EVI outputs including return intensity, range, Cartesian coordinates and radial distance that was defined as the horizontal component of range.

All scans were aligned to north using the reflective target, then six degree of freedom offsets between corner scans and the centre scan were determined manually by interactively shifting and rotating the point clouds, acknowledging that automated routines for coregistration already exist (e.g. Gruen and Akca, 2005). A Digital Elevation Model (DEM) and Canopy Height Model (CHM) were created using co-registered data of five scans per plot and using a grid cell size *G* (40 cm) and smoothing using a 1.5m Gaussian kernel (σ_K=1m) in accordance with values previously used in similar forest types (Ferster et al. 2009). Additionally, local maxima were derived from the CHM using the level set method (e.g. Kato et al. 2009) and a Parametric Height Model (PHM) was created using these local maxima and the CHM (Van Leeuwen et al. 2010). The PHM model outlines individual crowns by fitting cones to a CHM or to raw LiDAR data so that the number of returns within threshold distance *m* (10cm) from the cone surface is maximized. Transmittance of the DEM was set to zero. A list of variables and symbols used in the modeling is presented in table 1.

Subsequent processing addresses the detection of stem locations and the retrieval of stem diameters (§2.3.2.), and the derivation of geometric models of the forest plots (§2.3.3.). The virtual plots are then used to simulate canopy radiation transmission (§2.3.4.).

2.3.2. Stem detection and reconstruction

Tree stems were segmented from single scans. The segmentation was implemented using the Medial Axis Transformation (MAT) and regression analysis of object boundaries. The medial axis of a polygonal or polyhedral shape is a thin curve or curved plane centred within the boundaries of that shape (Das et al. 2011; Yuan et al. 2011; Martinez-Perez et al. 1999). A large number of methods exist for the derivation of the MAT (Siddiqi and Pizer 2008). In this study, the MAT was derived from a distance transformation. First, using radial distance, solid objects such as stems, branches, and ground hits were crudely separated from permeable targets (foliage) by identifying pixels whose range did not deviate from all 8-connected neighbouring pixels by more than a tolerance, δ (figure 1, step 1). In this binary image, apparent edges in the range image are zero while surfaces in the range image are non-zero. Second, from this binary image the Distance Transformation (DT) was computed (figure 1, step 2) that represents the distance from any surface pixel to their nearest edge pixel (e.g. Shih and Pu, 1995). Segments of surface pixels in the DT show an elevation in values towards the segment centres, resulting in the appearance of ridge-lines along the long axis of tree stems. Third, the MAT was derived from the distance transformed image using the sign-change of the image derivative that was computed along image lines (Siddiqi and Pizer 2008) (figure 1, step 3). Association of surface pixels to their nearest edge pixels allows for the conversion from a medial representation (MR) to a boundary representation (BR) (Siddiqi and Pizer 2008) (figure 1, step 4). A set of boundary pixels was obtained and classified into P_{left}, and P_{right} relative to the medial axis (P_{MAT}). An illustration of the method for stem detection is provided in figure 3.

Tree stems were detected using the MR and BR based on three filtering criteria: 1) a measure of normalized cross-correlation, *r*, between the paired boundary lines, 2) change in local orientation along the medial axes, ξ, and 3) the number of pixels contained in the medial axis, *n* (Fig 1, step 5). The normalized cross-correlation, *r*, was computed between corresponding pixel y-coordinates of the paired boundary lines:

$$\sum_j^k \frac{(P_{left,y,j} - \overline{P_{left,y}})(P_{right,y,j} - \overline{P_{right,y}})}{\sigma_{P_{left,y}} \cdot \sigma_{P_{right,y}} \cdot k} \qquad \text{(eq. 1)}$$

where *k* is the number of paired boundary pixels associated with the medial axis and $\sigma_{P_{left},y}$, $\sigma_{P_{right,y}}$ the standard deviations of y-coordinates. The normalized cross correlation is frequently used in image processing and computer vision, for example, to match stereo pairs (Fua 1993). The local orientation was computed for every medial axis pixel as the slope, in the image coordinate frame, of the line through the associated, paired boundary pixels ($P_{left,j}$, $P_{right,j}$). The parameter ξ was computed as the change of orientation between two adjacent medial axis pixels ($P_{MAT,j}$, $P_{MAT,j+1}$) and medial axis pixels for which the local orientation changed by more than a user specified threshold were removed. After filtering for ξ, the parameter *n* was used to filter any small objects that were considered too short to reliably compute a normalized cross-correlation. Filtering for r, ξ, and *n,* detects tree stems. A sensitivity analysis around stem detection parameters was conducted by varying one parameter at a time over specified ranges (Appendix 2.1.). Stem diameters were computed along unobscured, detected stems following Strahler et al. (2008):

$$t = \sin(\alpha_{span}/2) = \frac{D/2}{R+\frac{D}{2}} \quad \text{(eq. 2)}$$

$$D = 2R\frac{t}{1-t} \quad \text{(eq. 3)}$$

where *R* is the range, *D* the stem diameter, and α_{span} is the angular width spanned by the tree trunk. Stem centres were computed from the original radial distance that relate to the stem surface (i.e. bark), and derived stem diameters.

2.3.3. Mesh modeling

Stem segments detected in the single scans, that overlapped in co-registration were merged into a single stem object. To reduce impacts of co-registration errors as well as errors in diameter attribution between scans, the merged data were smoothed by averaging stem attributes along 0.5 m height intervals. Gaps in stem representation may occur, however, due to the effects of occlusion in ground-based laser scanning data. To bridge these gaps, B-splines were fitted through all stem segments (Dierckx 1993) and tangent vectors were computed at every spline node. For every possible pair of segments, a connecting spline was fitted using the same nodes as contained in the individual splines combined, and from the paired nodes the angles (*s*) between tangent vectors (connecting spline vs. the two separate splines) were computed, except for a number of six nodes centered around the joint of the two segments, due to sensitivity of splines towards the extremes (Daniels et al. 2008). If a pair of segments was shorter than six nodes in length, the pair was skipped. If these angles or the z-component of the gap length (L_Z) exceeded user specified values s_{MAX}, $L_{Z,MAX}$, respectively, the two segments were interpreted as not belonging to the same tree. Alternatively, any two segments were assessed to belong to the same tree stem if segment w_j was the smoothest connecting segment for w_i and if w_i was the smoothest connecting segment for w_j too; this is analogous to stereo matching criteria used in Fua (1993).

After this step, data occlusion near the trunk base and tree top may remain. To recover these final missing parts, an approach was developed where the trunks were extended towards the ground and the tree tops. Liu et al. (2005) describe an approach that reconstructs curves from point cloud information based on the tangential flow. Their algorithm produces a B-spline that grows along its two end-points using a cylinder that is aligned with the spline's tangent and that is used to follow apparent curves in the point cloud. Given that tangential vectors of trees are generally vertical, a solution of reduced complexity was sought in this study. The point cloud was compressed along the z-axis (i.e. height-axis) by a factor 20 and a cylinder with radius 2.5 m was placed around the top of the detected stem segment. Iteratively, the nearest return within 30 cm above the stem top and within the cylinder was added to the sequence of spline nodes and using the new top additional returns were added until no additional returns were found. The same procedure was used to extend the stem segments towards the ground.

The set of cones derived from the PHM, each representing an individual, dominant tree crown, was matched with the tree stems by locating, for every cone tip, the nearest stem top and for every stem top the nearest cone tip. If matches were mutual, a connection was registered (Fua, 1993). Stem diameters were then assigned using linear extrapolation towards the stem tops, while diameters were kept constant towards the DEM. The transmittance of the stems and the forest floor was set to zero.

Tree crowns were modeled using a combination of laser derived crown dimensions and Arbaro, an open source tree modeling software (Weber and Penn, 1995) that provides for the modeling of deciduous, coniferous, as well as herbaceous vegetation. Plants modeled in Arbaro behave as if they were solitary, and do not exhibit competition for light with neighboring vegetation. Arbaro uses an extensive list of parameters including branch lengths in relation to parent branches, the number and curvature of branches, as well as random variations around each parameter. To reduce the number of modeling parameters, no random variation was considered and a template coniferous tree crown was created whose dimensions and shape could be adapted to fit the stem shapes and crown outlines derived from the point clouds. The template tree was defined with a crown depth of 60% of tree height and a constant internode distance (0.25 cm), and a distribution of branch insertion angles and branch curvature that resemble the plagiotropic and heliotropic distribution of branches in the lower and top canopy strata, respectively (Hallé et al. 1978). Crown depth was estimated from field observations of dominant trees and was computed as the height of first living branch to the total tree height. Internode distance was chosen to balance the frequency of first order branching with computing resources, while ensuring that canopy layering was abundantly sampled. Heights and opening angles of cones in the PHM were used to define tree height and lengths of first order branches and the crowns were draped over the laser-reconstructed stems to account for sweep and lean. To avoid crowns intersecting one another and to ensure they resemble natural competition in stands, branches were scaled to individual tree growing spaces that were computed by tessellating the plot space to the nearest tree stem based on the rationale that locations within the plot are likely to be populated by foliage from the nearest stem, rather than a stem located further away. To simplify canopy representation without comprising the radiative consistency, clumping of foliage around each branch was abstracted from the Arbaro output by fitting planar polygons to clusters of first and second order branches. The use of planar surfaces to represent clumping of shoots around branches builds on traditional concepts used in layered crown and canopy models (Ross and Marshak 1991; Oker-Blom et al. 1991) and retains information about shoot normal angle distributions. After reconstruction of the plots, the mesh models were decimated to 50,000 triangles to reduce computing costs of radiative transmission simulations (§2.3.4.).

Uncollided transmission of radiation through the planar polygons was expressed as the gap fraction, $g(\vartheta_i)$, a measure similar to the foliage silhouette to total area ratio used in modeling shoot level albedos (Stenberg et al. 1995). This gap fraction is a function of illumination geometry relative to the normal angles of the branch facets. For incoming rays under a 0° normal angle, the gap fraction was set to 15% based on photographical measurements perpendicular to the predominant shoot direction that generally ranged between 10 to 20%, and the value of gap fraction decreased linearly with the cosine of the ray-normal-angle. The sensitivity of this parameter was assessed by changing $g(\vartheta_0)$ from 5 to 30% in steps of 5% (Appendix 2.2.).

2.3.4. Modeling the internal canopy radiation regime

The radiative consistency of the produced mesh model was validated against EVI derived measurements of gap probability (Jupp et al. 2009). Gap probability, $P_{gap}(\theta,R)$, is the probability of having no scattering material (e.g. foliage, woody material) between the laser scanner and a point at a specified range (R) under a specified zenith angle (θ) and is derived as:

$$P_{gap}(\theta,R) = 1 - \frac{1}{\rho_a}\int \rho_{app} \cdot r \cdot dr \qquad \text{(eq. 4)}$$

Where ρ_a is the normal reflectance of a face and ρ_{app} is the apparent reflectance that is determined from the recorded waveform of returned light energy as:

$$\rho_{app} = \frac{I(R,\theta) \cdot R^2}{K(R) \cdot \Phi_0} \qquad \text{(eq. 5)}$$

Where $I(R,\theta)$ is the measured intensity at the range R, and angle θ. K(R) is a telescope efficiency factor and Φ_0 is the outgoing energy (Jupp et al. 2009). P_{gap} is computed in zenith angle bands that are typically between 5 to 20° in width. A vertical profile of P_{gap} was computed from eq. 4 for each plot using the center scans. P_{gap} provides for the derivation of foliage profiles as:

$$L'(z) = -\log\left(P_{gap}'(z)\right) \qquad \text{(eq. 6)}$$

Foliage profiles were computed for zenith angles ranging from 55 to 60 degrees (Lovell et al. 2003) and were compared against the vertical distribution of facet areas of the mesh models. Vertical profiles of gap probability were derived from the mesh models by forward ray tracing (Appendix 2). Hemispherical irradiance was simulated using 5000 light sources that each emitted a single beam of collimated light directed towards the plot origin. The number of light sources was to balance the resolution of directional variation in hemispherical illumination such as caused by cloud cover, with computational cost of the model simulations (one light source corresponds to 1.26 milli-steradians). In this study, a 100% diffuse sky was simulated by assigning equal intensities to all light sources, and this relates to the condition of a complete overcast. At every ray-mesh intersection, the probability of uncollided transmission, *T*, through the facet (i.e. ground, stem, foliage) was determined from the directional gap fraction, $g(\vartheta_i)$, (§2.3.3) using the angle between the ray and the normal angle of the intersected face. At every intersection, Phit was computed as $(1-T) \cdot E_i$ and the propagated, uncollided irradiance as $T \cdot E_i$. Vertical hit distributions were derived as the fraction of hits within 10 cm height bins and were compared with the EVI P_{gap} profiles derived from a below-canopy perspective. As indication of correspondence, 50 samples at heights ranging between 0 – 30 m were randomly drawn from the simulated and full waveform derived P_{gap} profiles centered at 57.5° and Pearson correlation coefficients were computed for each plot. The processing pipeline is summarized in figure 2.

3. Results

3.1. Stem detection

Stem detection was calculated on average within 3 to 5 seconds per scan, making the technique extremely computationally efficient. The threshold parameters used for stem detection were $\delta=0.30$ *m*, $r=0.95$, $\xi=15°$, and $n=24$. Detection was limited to stems covering a minimum cross section of 3 to 4 pixels. Figure 4 shows the detection rate by radial distance measured over all 20 scans, from which cumulative detection rates can be obtained through integration. For distances up to 10 m, 93% of trees were detected. In general, trees not detected within 10 meters showed excessive branching, or were snags. At distances up to 15 m, 85% of trees were detected, while at distances up to 20 and 25 m only 67% and 56% of the trees were detected, respectively. This rapid reduction in detection rate with distance is a result of decreasing spatial point density with distance and effects of occlusion. Using the co-registered data, an average of 9.25 trees per plot totaling 9.8 % of trees detected in the field inventory were not located in the EVI derived stem map as a result of occlusion or decreasing resolving power with range. The method was insensitive against returns obtained from branches, albeit trees around this geographical location generally have sparse branch densities along the lower bole sections. The method was unable to detect some younger trees with heavy branching structure and foliage along the entire visible stem, and distant trees. Errors of commission were few and limited to objects close to the scanner and were eliminated later in the modeling pipeline as stems need to have a certain length. DBH estimates were found to correlate well with field observations (R^2 = 0.82; figure 5); However, a decrease in accuracy was observed, as expected, with distance from the scanner. Field measured DBH was underestimated ($p < 0.05$) by EVI ($\overline{EVI_{DBH}}$ = 22.5 cm vs. $\overline{Field_{DBH}}$ = 27.3 cm), consistent with findings of Strahler et al. (2008) and Yao et al. (2011). Figure 6 shows field detected and EVI detected tree stems for plot 1, with the size of the markers representing DBH. Mis-registration between compass (vertex) determined tree locations and EVI derived stem locations may be attributed to individual scanner setups as well as distance from the plot centre.

3.2. Mesh modelling

Accuracy of the stem modelling was assessed by interpreting the co-registered point clouds, and showed that the merging of individually detected tree stems and stem parts overcame many of the major issues associated with occlusion. Figure 7 provides an illustration of the stem reconstructions and shows that stems were modelled well into the higher strata of the canopy allowing consistent matching with the individual crown tops. In some cases, however, coregistration-errors caused that individual trees could not be correctly merged for the final mesh model, and these cases resulted in the reconstruction of two stems, instead of one. The implications of this on the formation of tree growing spaces seemed minimal as the combined set of growing spaces for these trees and their reconstructed crowns would act in the same manner as that it would for a single tree (Morsdorf et al. 2004). The creation of tree growing spaces was effective in delineating both dominant as well as suppressed trees (data not shown). The method does not guarantee that individual branches always get assigned to their true parent stem. In all cases, however, the foliage gets assigned to their nearest stems. In figure 8, a demonstration is provided of the fitting of planar polygons to the crowns of the Arbaro tree models, the fitting the modelled crowns to the reconstructed tree stems, and scaling of the crowns to the growing spaces. Figure 9 shows the reconstructed virtual forest plots using the Arbaro tree models parameterized with tree height, and crown taper, that were derived from the EVI data set. The Arbaro tree model output coarsely resembled the clumping of foliage around branches and into crowns, typical for conifers (Oker-Blom 1986), although the exact placement of foliage material could not be validated at tree level against the current data set.

It was found across all plots that tree heights in the mesh model were considerably shorter than field measured heights; this is also reflected in figure 10 showing facet area profiles of the mesh models against height vs. EVI derived leaf area profiles against height. Some of this underestimation may be explained from decreasing ability to detect discrete returns with increasing path length through the canopy, while additional contributions were associated with the creation of the CHM, and PHM, and decimation of the Arbaro tree crown models that resulted in the removal of fine branches located at the tree tops. In contrast to the EVI foliage profiles, the facet area profiles include a profound ground peak that is due to the inclusion of the ground terrain in the mesh models. Significant differences between foliage profiles and facet area profiles remain for the mid-canopy (around 15m) that can be explained from differences in definition between these two profiles and that may be resolved by foliage density attribution to the individual facets.

3.3. Modeling radiative transmission properties

Figure 11 shows the modeled hit distribution against height. Individual data points represent fractions of hits within 10 cm height bins, while the fitted lines show a polynomial fit and moving median (1 m window size) through these data points. A sixth order polynomial fit was chosen to capture peaks in absorption by the canopy volume as well as ground vegetation. Simulated hit distributions showed an increase around the mid-canopy where foliage and facet area densities are highest and also showed increasing variation in light interception with canopy depth (figure 11). The highest probability P_{hit} for single facets was observed near the tree tops and around canopy gaps.

Vertical profiles of P_{gap} were computed using zenith angles centered around 17.5°, 27.5°, 37.5°, 47.5°, and 57.5° using a 5° bandwidth (figure 12). A strong dependence of the P_{gap} profiles on the zenith angle was observed. For larger zenith angles, values of P_{gap} were considerably smaller than corresponding values at smaller angles as a result of path length through the canopy. Figure 12 also shows the simulated hit distribution profile as a function of height (thicker black line) and shows consistent behavior with trends in the full waveform derived profiles. The Pearson correlations coefficient computed between 50 random samples taken from the simulated hit distribution and full waveform P_{gap} distribution centered at 57.5° was 0.97, 0.95, 0.97 and 0.91 for plot 1, 2, 3, and 7, respectively ($P << 0.01$). A noticeable difference is observed at heights over 20-25 m that can be addressed to the difference in illumination geometries between the real and simulated results. While the EVI has a below-canopy perspective, the simulated results are obtained from an overhead perspective and resemble the down welling radiation from the sky.

4. Discussion and conclusions

4.1. Stem detection

The presented method for stem detection provided accurate results in a highly computationally efficient approach and provides an alternative solution to circle fitting approaches (e.g. Maas et al. 2008) with a comparative advantage for lower resolution data sets (e.g. 0.25° angular resolution). Application of the method to commercial, discrete return scanners and datasets derived from stereo cameras or low-cost, triangulation-based range cameras (Dal Mutto et al. 2012) should be investigated. Through simultaneous localization and mapping (SLAM) these data may – in future – be merged to recover 3D maps covering extensive areas (Nuchter et al. 2007). Future research will also apply stem detection to deciduous species with more complex branching structures. A current concern is that the 3x3 kernel test effectively erodes the width of the trunk that has important impacts on diameter retrieval, which may be mitigated through incorporating other algorithms such as connected component labeling that preserved contours in the segmented image. Stem detection was insensitive to the parameter ξ for a large number of scans, hence reproduction over a range of forest types may reveal if this parameter could be omitted or its function substituted, for example, by a bivariate regression filter, instead of the current univariate correlation r.

4.2. Mesh modeling

Architectural tree modelling software has predominantly been used within the fields of computer graphics and visualization and only more recently in remote sensing and image processing (Widlowski et al. 2007b, Côté et al. 2009). Challenges in adopting these models in remote sensing largely relate to the parameterization that is geared towards graphical display rather than physiological functioning (see also table 2 for a comparison). Arbaro provides for the modelling of a large variety of tree species from coniferous to broadleaved trees and grasses through a common set of variables. A modification of Abraro was used in this study with an emphasis on physiological functioning and radiation transfer by modelling branches as planar polygons that possess the average radiation attributes derived from field observations. The model parameterizations required default settings that were considered species-specific, and effects of stocking density and age on the radiative characteristics of the foliage needs to be further investigated. The current implementation is of a modular form that allows substitution of field observations with laser derived geometrical attributes. For example, shoot level structure acquired through laser scanning of shoot samples can be included in the canopy representation as attribute data or can be used to substitute the planar polygons entirely, for example for establishing benchmark scenes for model intercomparison (Widlowski et al. 2007a).

The abstraction of crown architecture to meet computation power and functional representation is a key challenge that needs to be addressed in forming radiative transfer models that need to be operated over considerable spatial scales or where extensive analysis of parameter sensitivity is required using conventional computer hardware. The current choice of using planar polygons closely resembles the organization of foliage into layers that has been frequently used for modeling radiative transfer (Marshak and Ross 1991); However, other abstractions such as shoot cylinders (Oker-Blom et al 1991) or convex volumes of foliage (Strahler and Jupp, 1991) could be applied to pine or a broad variety of deciduous species. Abstracting the actual crown morphology introduces, however, model parameters that are effective in describing canopy radiation (e.g. Asrar and Myneni, 1991), yet their actual real-life meaning is lost. An example of such a parameter is the effective LAI that provides for the application of Lambert-Beer's Law to clumped canopies, but its value does not equate to the real canopy LAI. The current processing pipeline attempts to address concerns around the use of effective parameters by avoiding them where possible and adopting easy-to-measure forest inventory parameters relating to stem and crown dimensions and –architecture.

While of less importance in radiative transfer modeling, stem locations form a significant aspect in the current automation pipeline (Côté et al. 2009) as stems are used to segment the plot into individual tree growing spaces and constrain the distribution of foliage elements. It is anticipated that the presented modeling pipeline works equally for other species that have a monopodial trunk. For species with trunks that split into different directions, a similar processing pipeline can be envisioned where growing spaces are derived around the individual stems and branches and scaling of the tree regenerations revolves around these individual growing spaces. For these cases, a similar ordering of parameter sensitivities as listed in the Appendix may be expected in that lower order stems have greater influence on the radiation profile, yet further research is needed to confirm these assumptions. Future studies may also investigate the use of tree (stem) vigor and dominance as weighing criteria in defining growing spaces, as well as adaptation of foliage densities and biophysical properties to the modeled radiation regime (Côté et al. 2011).

4.3. Radiative transmission

This paper presents a reconstruction method with which 3D explicit models were derived from a point cloud of a coastal Douglas fir forest. From these models, the range to first hit for a given irradiation geometry can be studied and compared with full waveform derived P_{gap} measurements (Jupp et al. 2009). A widely accepted theory on radiation transmission in forest canopies is based on the Lambert-Beer law that prescribes the exponential decrease in radiation with canopy depth and assumes a random distribution of foliage material and a homogeneous layering of foliage. Under these assumptions, P_{gap} profiles show an exponential decrease with the optical depth of the canopy and this principle is also observed in our model simulations. At spatially finer scales large deviations from the idealized Lambert-Beer concept are expected (e.g. De Pury and Farquhar, 1999) which is also observed in our model. Yet, how well the current model represents the fine spatial radiation patterns of the real forest canopy could not be assessed with the current data set.

The EVI P_{gap} profiles corresponding to larger zenith angles show a convex shape owing to the increase in path length and reflect that information about canopy structure enclosed in the EVI data is biased towards lower canopy strata (Hilker et al. 2010b). Too small a zenith angle is prohibitive, however, as the occurrence of canopy gaps is biased towards the zenith (Yang et al. 2010). It is thus assumed that the range of zenith angles used in this study provides a level of confidence around the true plot-level P_{gap}. Figure 12 shows that P_{gap} approaches values close to zero towards the canopy top. This is due to the stand reaching canopy closure and for more open canopies the values of P_{gap} may be much larger (Yang et al. 2010). All plots show a strong similarity in P_{gap} profiles indicative of the homogeneity of the stand. A maximum in the hit distribution can be observed for heights around 15 m, as well as a ground peak that contributes to around 5 to 10% of total incident radiation. Plot 7 shows the fastest increase in hit distribution with canopy depth, albeit subtle, which may be explained from its nitrogen enrichment.

Validation of our mesh reconstruction was achieved against the EVI Pgap profiles and results indicate strong correlations between the hit distributions derived from the mesh reconstructions and full waveform Pgap profiles. For a correct interpretation of these results, the differences between the Pgap and hit distributions should be considered, however. The main difference between our simulation and EVI Pgap is the geometry of illumination; while the ray tracing simulations illuminate from the top of the canopy downward, the EVI data is collected from a below-canopy perspective. Although simulations could use the identical illumination geometry as the EVI, this was not done for two reasons: 1) The current processing pipeline is limited in modeling the bottom of forest canopies, and for simulations with a below-canopy perspective the parts of the canopy closer to the instrument set-up would attract a greater influence on the modeling results. 2) Moreover, from a physiological perspective it is more interesting to simulate irradiance from the top of canopy downwards as the largest contribution to forest productivity is provided by higher canopy strata. The difference in illumination geometry may be resolved through the use of tower-based scanning instruments (Eitel et al. 2012).

Future research should primarily address the tuning of parameter values to a range of forest types, species and age compositions, as well as resolving scaling issues and transfer of the presented method to other instruments. The limited size of the current research plot introduces edge affects that impact the hit distributions in that larger portions of radiation are received at lower heights compared to what would have been absorbed if the plot was not isolated from its environment. These edge effects need to be addressed through acquisition of laser scanning data over larger areas (e.g. 100 x 100 m) or by using subsamples of extensive wall to wall airborne LiDAR data sets. In addition, results of the current study are simulated at plot level, although computations include approximations at a much finer scale. Future work will examine the three dimensional consistency of radiative transfer at around a $1m^3$ scale against an *in situ* sensor network that captures diurnal as well as seasonal changes in canopy radiation and narrow waveband data that relate to the efficiency of solar energy capture and primary production (Garrity et al. 2009). Future research is also needed to investigate the influence of stocking density, crown dimensions and foliage distributions on the evolution of the canopy radiation regime with stand development and its implications for forest growth and management.

5. Acknowledgements

We would like to express our thanks to members of the Integrated Remote Sensing Studio, members of the Biometerology and Soil Physics Group, Dr. Andrew Black and Zoran Nesic, University of British

Columbia for their assistance with the field work, and four anonymous reviewers for their constructive feedback as well as Dr. Widlowski for advice regarding ray tracer validation. Parts of this research are funded by an NSERC Discovery grant to Dr. Coops. Additional funding was received from the Government of Canada through the Lodgepole Pine Partnership Project funded by the Canadian Forest Service and the Canadian Wood Fibre Centre.

6. References

Andrieu, B., Sohbi, Y., & Ivanov, N. (1994). A direct method to measure bidirectional gap fraction in vegetation canopies. *Remote Sensing of Environment, 50*, 61-66.

Arecchi, A. V., Messadi, T., & Koshel, R. J. (2007). Field Guide to Illumination. Bellingham, WA: SPIE Press.

Aschoff, T., Spiecker, H. (2004). Algortihms for the automatic detection of trees in laser scanner data. *International Archives of the Photogrammetry, Remote Sensing and Spatial Information Sciences XXXVI, part 8/W2*, 71-75.

Asrar, G., Myneni, R.B. (1991). Applications of Radiative Transfer Models for Remote Sensing of Vegetation Conditions and States. In R.B. Myneni, & J. Ross (Eds.), *Photon-Vegetation Interactions: Applications in Optical Remote Sensing and Plant Ecology* (pp. 538-558). Berlin Heidelberg: Springer-Verlag.

Bucksch, A., Lindenberg, R., Menenti, M. (2010). SkelTre – Robust skeleton extraction from imperfect point clouds. *Visual Computer, 26*, 1283-1300.

Côté, J.-F., Fournier, R.A., & Egli, R. (2011). An architectural model of trees to estimate forest structural attributes using terrestrial LiDAR. *Environmental Modelling and Software, 26,* 761-777.

Côté, J.-F., Widlowski, J., Fournier, R.A., & Verstraete, M.M. (2009). The structural and radiative consistency of three-dimensional tree reconstructions from terrestrial LiDAR. *Remote Sensing of Environment, 113,* 1067-1081.

Daniels, J., Ochotta, T., Ha, L.K., & Silva, C.T. (2008). Spline-based feature curves from point-sampled geometry. *Visual Computer, 24,* 449-462.

Das, S., Mirnalinee, T.T., & Varghese, K. (2011). Use of salient features for the design of a multistage framework to extract roads from high-resolution multispectral satellite images. *Transactions on Geoscience and Remote Sensing, 49,* 3906-3931.

De Pury, D. G. G., & Farquhar, G. D. (1997). Simple scaling of photosynthesis from leaves to canopies without the errors of big-leaf models. Plant, Cell and Environment, 20, 537–557.

Dierckx, P. (1993). Curve and surface fitting with splines, Monographs on Numerical Analysis. Oxford University Press.

Eitel, J.U.H., Vierling, L.A., Magney, T.S. (2012). Autonomously operating terrestrial laser scanner for monitoring forest ecosystems at a very high temporal resolution. Silvilaser, 16-19 Sept. 2012, Vancouver, Canada, Paper Number: SL2012-176.

Ferster, C.J., Coops, N.C., & Trofymow, J.A. (2009). Above-ground large tree mass estimation in a coastal forest in British Columbia using plot-level metrics and individual tree detection from LiDAR. *Canadian Journal of Remote Sensing, 35*, 270-275.

Field, C. (1983). Allocating leaf nitrogen for the maximization of carbon gain: leaf age as a control on the allocation program. *Oecologia, 56*, 341-347.

Fleck, S., Van der Zande, D., Schmidt, I., & Coppin, P. (2004). Reconstruction of tree structures from laser-scans and their use to predict physiological properties and processes in canopies. *International Archives of the Photogrammetry, Remote Sensing and Spatial Information Sciences XXXVI, part 3/W52*, 125-129.

Fua, P. (1993). A parallel stereo algorithm that produces dense depth maps and preserves image features. *Machine Vision and Applications, 6*, 35-49.

Garrity, S.R., Vierling, L.A., & Bickford, K. (2010). A simple filtered photodiode instrument for continuous measurement of narrowband NDVI and PRI over vegetated canopies. *Agricultural and Forest Meteorology,* 150, 489-496.

Givnish, T. (1988) Adaptation to sun and shade: A whole-plant perspective. *Australian Journal of Plant Physiology, 15*, 63-92.

Gruen, A., Akca, D. (2005). Least squares 3D surface and curve matching. *ISPRS Journal of Photogrammetry and Remote Sensing*, *59*, 151-174.

Hallé, F., Olderman, R.A.A., Tomlinson P.B. (1978). *Tropical Trees and Forests. An Architectural Analysis.* Berlin: Springer-Verlag.

Hilker, T., Hall, F.G., Coops, N.C., Lyapustin, A., Wang, Y., Nesic, Z., Grant, N., Black, T.A., Wulder, M.A., Kljun, N., Hopkinson, C., Chasmer, L. (2010a). Remote sensing of photosynthetic light-use efficiency across two forested biomes: Spatial scaling. *Remote Sensing of Environment, 114,* 2863-2874

Hilker, T., Lepine, L., Coops, N.C., Jassal, R., Black, T.A., Wulder, M.A., Ollinger, S.V., Tsui, O., Day, M. (2012) Assessing the impact of N-fertilization on biochemical composition and biomass of a Douglas-fir canopy - a remote sensing approach. *Agricultural and Forest Meteorology, 153*, 124 – 133.

Hilker, T., v. Leeuwen, M., Coops, N.C., Wulder, M.A., Newnham G., Jupp D.L.B., & Culvenor D.S. (2010b). Comparing canopy metrics derived from terrestrial and airborne laser scanning in a Douglas-fir dominated forest stand. *Trees - Structure and Function, 24,* 819-832.

Humphreys, E.R., Black, T.A., Morgenstern, K., Cai, T.B., Drewitt, G.B., & Nesic, Z. (2006). Carbon dioxide fluxes in coastal Douglas-fir stands at different stages of development after clearcut harvesting. *Agricultural and Forest Meteorology, 140,* 6-22.

Jacquemoud, S., Verhoef, W., Baret, F., Bacour, C., Zarco-Tejada, P.J., Asner, G.P., Francois, C., & Ustin, S.L. (2009). PROSPECT + SAIL: A review of use for vegetation characterization. *Remote Sensing of Environment, 113,* s56-s66.

Jassal, R.S., Black, T.A., Spittlehouse, D.L., Brummer, C., & Nesic, Z. (2009). Evapotranspiration and water use efficiency in different-aged Pacific Northwest Douglas-fir stands. *Agricultural and Forest Meteorology, 149*, 1168-1178.

Jupp, D.L.B., Culvenor D.S., Lovell J.L., Newnham G.J., Strahler A.H., & Woodcock, C.E. (2009). Estimating forest LAI profiles and structural parameters using a ground-based laser called 'Echidna'. *Tree Physiology, 29,* 171–181.

Kato, A., Moskal, L.M., Schiess, P., Swanson, M.E., Calhoun, D., & Stuetzle, W. (2009). Capturing tree crown formation through implicit surface reconstruction using airborne lidar data. *Remote Sensing of Environment, 113*, 1148-1162.

Liang, X., Litkey, P., Hyyppa, J., Kaartinen, H., & Vastaranta, M. (2012). Automatic stem mapping using single-scan terrestrial laser scanning. *IEEE Transactions on Geoscience and Remote Sensing, 50*, 661-670.

Liu, Y., Yang, H., & Wang, W. (2005). Reconstructing B-spline curves from point clouds – A tangential flow approach using least squares minimization. *ACM Transactions on Graphics, 25*, 214-238.

Lovell, J.L., Jupp, D.L.B., Culvenor, D.S., & Coops, N.C. (2003). Using airborne and ground-based ranging LiDAR to measure canopy structure in Australian forests. *Canadian Journal of Remote Sensing, 29*, 607-622.

Maas, H.-G., Bienert, A., Scheller, S., & Keane, E. (2008). Automatic forest inventory parameter determination from terrestrial laser scanner data. *International Journal of Remote Sensing, 29,* 1579–1593.

Mariscal, M.J., Martens, S.N., Ustin, S.L., Chen, J., Weiss, S.B., & Roberts, D.A. (2004). Light-transmission profiles in an old-growth forest canopy: simulations of photosynthetically active radiation by using spatially explicit radiative transfer models. *Ecosystems, 7,* 454-467.

Martinez-Perez, M., Hughes, A., Stanton, A., Thom, S., Bharath, A., & Parker, K. (1999). Retinal blood vessel segmentation by means of scale space analysis and region growing. In C. Taylor, & A. Colchester (Eds.), Medical image computing and computer-assisted intervention – MICCAI'99 (pp. 90-97). Berlin Heidelberg: Springer.

Möller, T., Trumbore, B. (1997) Fast, minimum storage ray-triangle intersection. *Journal of Graphics Tools*, *2*, 21--28.

Morgenstern, K., Black, T.A., Humphreys, E.R., Cai, T., Drewitt, G.B., Gaumont-Guay, D., Griffis, T.J., Jork, E.-M., & Nesic, Z. (2004). Sensitivity and uncertainty of the carbon balance of a Pacific Northwest Douglas-fir forest during an El Niño/La Niña cycle. *Agricultural and Forest Meteorology, 123*, 201-219.

Morsdorf, F., Meier, E., Kötz, B., Itten, K.I., Dobbertin, M., Allgöwer, B. (2004). LIDAR-based geometric reconstruction of boreal type forest stands at single tree level for forest and wildland fire management. *Remote Sensing of Environment, 92*, 353-362.

Oker-Blom, P. (1985). The influence of penumbra on the distribution of direct solar radiation in a canopy of Scots pine. *Photosynthetica, 19*, 312-317.

Oker-Blom, P. (1986). Photosynthetic radiation regime and canopy structure in modeled forest stands. *Acta Forestalia Fennica, 197*, 1-44.

Oker-Blom, P., Lappi, J., Smolander, H. (1991). Radiation regime and Photosynthesis of Coniferous Stands. In R.B. Myneni, & J. Ross (Eds.), *Photon-Vegetation Interactions: Applications in Optical Remote Sensing and Plant Ecology* (pp. 441-467). Berlin Heidelberg: Springer-Verlag.

Parker, G.G., Lefsky, M.A., & Harding, D.J. (2001). Light transmittance in forest canopies determined using airborne laser altimetry and in-canopy quantum measurements. *Remote Sensing of Environment, 76*, 298-309.

Prusinkiewicz, P., & Lindenmayer, A. (1990). The algorithmic beauty of plants. New-York: Springer-Verlag.

Ross, J., & Marshak, A. (1991). Monte Carlo Methods. In R.B. Myneni, & J. Ross (Eds.), *Photon-Vegetation Interactions: Applications in Optical Remote Sensing and Plant Ecology* (pp. 441-467). Berlin Heidelberg: Springer-Verlag.

Runions, A., Lane, B., & Prusinkiewicz, P. (2007). Modeling trees with a space colonization algorithm. *Eurographics Workshop on Natural Phenomena 2007* (pp. 63-70).

Schaepman-Strub, G., Schaepman, M.E., Painter, T.H., Dangel, S., Martonchik, J.V. (2006). Reflectance quantities in optical remote sensing – definitions and case studies. *Remote Sensing of Environment 103*, 27-42.

Shih, F.Y. , & Pu, C.C. (1995). A Skeletonization algorithm by maxima tracking on Euclidean distance transform. *Pattern Recognition, 28*, 331-341.

Siddiqi, K., & Pizer, S.M. (2008). *Medial Representations: Mathematics, Algorithms, and Applications*. Berlin Heidelberg: Springer.

Stenberg, P., Linder, S., & Smolander, H. (1995). Variation in the ratio of shoot silhouette area to needle area in fertilized and unfertilized Norway spruce trees. *Tree Physiology, 15*, 705-712.

Stenberg, P. (1995). Penumbra in within-shoot and between-shoot shading in conifers and its significance for photosynthesis. *Ecological Modelling, 77*, 215-231.

Strahler, A. H., & Jupp, D. L. B. (1991). Geometric-optical modeling of forests as remotely-sensed scenes composed of three-dimensional, discrete objects. In R. B. Myneni, & J. Ross (Eds.), Photon-vegetation interactions: Applications in optical remote sensing and plant ecology (pp. 415–440). Berlin-Heidelberg: Springer-Verlag.

Strahler, A.H., Jupp, D.L.B., Woodcock, C.E., Schaaf, C.B., Yao, T., Zhao, F., Yang, X.Y., Lovell, J., Culvenor, D., Newnham, G., Ni-Miester, W., & Boykin-Morris, W. (2008). Retrieval of forest structural parameters using a ground-based LiDAR instrument Echidna (R). *Canadian Journal of Remote Sensing, 34*, S426–S440.

Suffern, K.G. (2007). Ray tracing from the ground up. Wellesley, Massachusetts, 762 pp.

Van der Tol, C., Verhoef, W., & Rosema, A. (2009). A model for chlorophyll fluorescence and photosynthesis at leaf scale. *Agriculture and Forest Meteorology, 149*, 96-105.

Van der Zande, D., Stuckens, J., Verstraeten, W.W., Mereu, S., Muys, B., Coppin, B. (2011) 3D modeling of light interception in heterogeneous forest canopies using ground-based LiDAR data. *International Journal of Applied Earth Observation and Geoinformation, 13,* 792-800.

Van Leeuwen, M., Coops, N.C., & Wulder, M.A. (2010). Canopy surface reconstruction from a LiDAR point cloud using Hough transform. *Remote Sensing Letters, 1,* 125-132.

Verroust, A., & Lazarus, F. (2000). Extracting skeletal curves from 3D scattered data. *The Visual Computer, 16*, 15-25.

Wang, Y.P., & Jarvis, P.G. (1990). Description and validation of an array model – MAESTRO. *Agricultural and Forest Meteorology, 51*, 257-280.

Weber, J., & Penn, J. (1995). Creation and rendering of realistic trees. Proceedings of the 22nd annual conference on Computer graphics and interactive techniques SIGGRAPH (pp. 119–128). New York: ACM.

Welles, J.M., & Norman, J.M. (1991). Photon transport in discontinuous canopies: A weighted random approach. In R.B. Myneni & J. Ross (Eds.), *Photon-Vegetation Interactions: Applications in Optical Remote Sensing and Plant Ecology* (pp. 389-414). Berlin Heidelberg: Springer-Verlag.

Widlowski, J.-L., Pinty, D., Lavergne, T., Verstraete, M.M., & Gobron, N. (2006). Horizontal radiation transport in 3-D forest canopies at multiple spatial resolutions: Simulated impact on canopy absorption. *Remote Sensing of Environment, 103*, 379-397.

Widlowski J-L., Robustelli M., Disney M., Gastellu-Etchegorry J.-P., Lavergne T., Lewis P., North P. J. R., Pinty B., Thompson R. and Verstraete M. M. (2007a). The RAMI On-line Model Checker (ROMC): A web-based benchmarking facility for canopy reflectance models. *Remote Sensing Environment, 112,* 1144-1150.

Widlowski, J-L., Taberner, M., Pinty, B., Bruniquel-Pinel, V., Disney, M., Fernandes, R., Gastellu-Etchegorry, J.-P., Gobron, N., Kuusk, A., Lavergne, T., Leblanc, S., Lewis, P., Martin, E., Mottus, M., North, P.J.R. , Qin, W., Robustelli, M., Rochdi, N., Ruiloba, R., Soler, C., Thompson, R., Verhoef, W., Verstraete, M.M., & Xie, D. (2007b). The third RAdiation transfer Model Intercomparison (RAMI) exercise: Documenting progress in canopy reflectance modelling. *Journal of Geophysical Research, 112*, D09111, 28.

Yang, W., Ni-Meister, W., Kiang, N.Y., Moorcroft, P.R., Strahler, A.H., & Oliphant, A. (2010). A clumped-foliage canopy radiative transfer model for a global dynamic terrestrial ecosystem model II: Comparison to measurements. *Agricultural and Forest Meteorology, 150*, 895-907.

Yang, X., Strahler, A., Schaaf, C., Jupp, D., Yao, T., Zhao, F., Wang, Z., Culvenor, D., Newnham, G., Lovell, J., Dubayah, R., Woodcock, C., Ni-Meister, W. (in press). Three-dimensional forest reconstruction and structural parameter retrievals using a ground-based full-waveform lidar Instrument (Echidna). *Remote sensing of environment.*

Yao, T., Yang, X., Zhao, F., Wang, Z., Zhang, Q., Jupp, D., Lovell, J., Culvenor, D., Newnham, G., Ni-Meister, W., Schaaf, C., Woodcock, C., Wang, J., Li, X., & Strahler, A. (2011). Measuring forest structure and biomass in New England forest stands using Echidna ground-based lidar. *Remote Sensing of Environment, 115*, 2965-2974.

Yuan, J., Wang, D.L., Wu, B., Yan, L., & Li, R. (2011). LEGION-based automatic road extraction from satellite imagery. *IEEE Transactions on Geoscience and Remote Sensing, 49*, 4528-4538.

Appendix

A.1. Sensitivity Analysis

A.1.1. Stem detection

The sensitivity of stem detection to changes in parameter values was analysed using the plot-centre scans and varying one parameter over specified ranges (δ = 0.1, 0.2, 0.3, 0.4, 0.5 m; r = 0.7, 0.8, 0.9, 0.99, 0.995; ξ = 5, 10, 15, 20, 35°; n = 6, 12, 24, 36, 42), while the remaining parameters were kept fixed (δ = 0.3m; r = 0.95; ξ = 15°; n = 12) to capture commission and omission errors. Table 3 summarizes the sensitivity around δ, r, and n. Filtering for ξ only reduced errors of commission in some scans, whereas it had no effect in others including the plot-center scans.

A.1.2. Arbaro Parameters

A listing of the Arbaro parameters that were not derived from point cloud data is provided in table 4. The sensitivity of these Arbaro parameters on radiative transfer simulations was assessed by conducting a set of simulations using an arbitrary stem and tree height map, and changing Arbaro parameter values by +20% and -20% (in steps of 10%). One Arbaro parameter was changed at a time, while remaining parameters were kept constant. The sensitivity analysis shows that base size, defining the height of the branch free bole section and canopy depth, is the most sensitive parameter. First order down angle (1DownAngle) and its distribution (1DownAngleV) with canopy depth, both parameters regulating the angle between a branch and the main stem, causes estimates of cumulative hit distributions to vary by 16% and 8% of total absorbed radiation, respectively. The six most important Arbaro parameters were further investigated and the effect of individual parameters and their interactions are shown in figure 13. Along the diagonal the effect of changing one parameter is shown. The cumulative hit distribution using the reported values is presented by a thick line and the two thinner lines indicate the range in simulation outcomes caused by changing the respective parameter value. The upper half of the matrix lists these effects for changing two parameters at a time. The lower half of the matrix plots the range in simulation outcomes against canopy depth so that the black line in plots (i,j) correspond with plots (j,i) and the blue and red lines correspond with the plots along the diagonal. For example, a change in base size of +/- 20% (0.32 to 0.48) causes a change in the cumulative hit distribution from 0.18 to 0.47 around 21 m height, indicating the significance of this parameter on the derived hit distribution profiles. In addition, varying both the value of BaseSize and 1DownAngle simultaneously causes a greater range in model outcomes than changing either of the parameters alone. This effect is disaggregated to individual parameter contributions in the lower half of the matrix. The graphs show a decrease in parameter sensitivity with branching order.

A.1.3. Gap fraction

Besides the geometry of the mesh model, gap fraction is an important parameter regulating uncollided transmission through the planar polygons and thus the hit distribution. Varying $g(\vartheta_i)$ from 5 to 30% resulted in a maximum difference in hit distribution at 18 m of 0.02 suggesting that most transmission occurs between crowns and outside the branch silhouettes. Values used for $g(\vartheta_i)$ are among the lower bound observed for 30 year old Norway spruce in Sweden (Stenberg et al. 1995).

An analysis of the effects of varying foliage densities on the radiation transmission properties of the virtual canopies was conducted after separating sun and shade facets. This was achieved by computing for every facet in the scene the probability of a direct line of sight in directions from a set of 1,064 uniformly distributed directions across the hemisphere. Using computed sun azimuth and zenith angles, a stratification of facets into sun and shade was made based on whether the facets were in direct line of sight with the sun (Hilker et al. 2010a). The effects of different foliage densities on the hit distribution were then investigated by altering the gap fractions of sun and shade facets (Figure 14). The lower value is the gap fraction for sun facets and the higher value for shade facets. We can see that the impact of changing the effects of different foliage densities is small compared to some of the effects of other parameters in our model. This indicates that the crown shape is causing the observed radiation profiles, and to a lesser extent the foliage densities of the individual facets in the crowns.

A.2. Ray Tracer details

To provide a better understanding of the ray tracer developed for this study, this appendix provides a brief overview of its main components and underlying algebra of radiation transport.

A.2.1. Radiation Transport

When computing reflectance from a certain surface element into directions (φ_r, θ_r), the intrinsic scattering properties of the material under consideration in combination with the projected solid angle (Arecchi et al. 2007) are of principle importance. In the current ray tracer, reflectance and transmittance are described for a Lambertian surface, that is a surface that reflects the same amount of radiation [W m^{-2} sr^{-1}] in all directions, and its intensity [W m^{-2}] drops with the cosine normal angle (Schaepman-Strub et al. 2006). Thus, the probability of a photon hitting a Lambertian surface and reflecting (transmitting) in a certain direction is a probability density functions whose values decreases with the cosine of the angle between the incident path of the photon and the surface normal.

The bidirectional reflectance distribution function (BRDF) [sr^{-1}] of a surface describes the distribution of reflection over a hemisphere of outgoing directions (φ_r, θ_r) for a beam that is incident on the surface under direction (φ_i, θ_i). The BRDF is defined as the ratio of radiance L_r [W m^{-2} sr^{-1}] that is reflected from the surface and irradiance E_i [W m^{-2}] that is incident on the surface. For any given surface the BRDF integrated over the viewing hemisphere sums to the surface reflectance, ρ_d [unitless]. A Lambertian surface has a constant BRDF of ρ_d/π, so that when integrated over the full hemisphere (Suffern, 2007):

$$\int_{\phi=0}^{2\pi}\int_{\theta=0}^{\frac{\pi}{2}} f_{Lambert} \cdot sin(\theta) \cdot cos(\theta) \cdot d\theta \cdot d\phi \cdot dA =$$

$$2\pi \cdot \rho_d/\pi \cdot \int_{\theta=0}^{\pi/2} sin(\theta) \cdot cos(\theta) \cdot d\theta \cdot dA = 2\pi \cdot \rho_d/\pi \cdot \frac{1}{2} \cdot dA = \rho_d \cdot dA$$

The reflected radiance into any one direction (φ_r, θ_r) from such a surface is:

$$L_r = \frac{1}{\pi} \cdot \rho_d \cdot E_i = \frac{1}{\pi} \cdot \rho_d \cdot \int_{\omega} L_i \cdot dA \cdot cos(\theta_i) \cdot d\omega$$

Furthermore, it can be observed analytically that the reflected intensity of such a surface decreases with increasing normal angle:

$$\frac{d\Phi_r}{dA} = \frac{1}{\pi} \cdot \rho_d \cdot E_i \cdot cos(\theta_r) = \frac{1}{\pi} \cdot \rho_d \cdot cos(\theta_r) \cdot \int_{\omega} L_i \cdot dA \cdot cos(\theta_i) \cdot d\omega$$

The bidirectional reflectance of a Lambertian target can thus be described by the intensity of photons hitting a surface element and a cosine-weighted probability of reflecting into the direction (φ_r, θ_r). Transmittance is described similarly using a Bidirectional Transmittance Distribution Function (BTDF), that for a Lambertian target equals to $\frac{1}{\pi} \cdot \tau_d$, where τ_d is the materials collided transmittance.

A.2.2. Monte Carlo ray tracing

The ray tracer is implemented in the Python programming language, follows object-oriented coding design and was developed specifically for computing P_{hit} and P_{gap} but has been extended to compute absorptance and transmittance for model validation purposes. The ray tracer simulates absorptance and transmittance by tracing individual photon paths within a virtual scene of Lambertian targets that are all a circular or triangular shape. Intersections of photon paths with the scene elements are computed largely following Möller and Trumbore (1997) and methodology explained by D. Sunday (http://geomalgorithms.com/a06-_intersect-2.html). Photons originate from a reference plane that is oriented horizontally and that is just above the highest element in the scene. When photons collide with the scene elements, their fate as to being absorbed or scattered is evaluated from the materials properties ρ_d, and τ_d and in the case of either reflection or transmission a new direction vector is sampled from a cosine weighted hemispherical distribution (Suffern, 2007). A new photon is generated each time a previous photon is absorbed or bounced outside the scene. Alternatively, the ray tracer provides for the simulation of P_{hit} and P_{gap} by generating rays that upon intersection with the scene are partially obstructed and for which uncollided transmittance can be computed based on a gap fraction assigned to each surface element.

A.2.2.1. Validation

Validation of the ray tracer was achieved against the Radiative Transfer Model Intercomparison (RAMI) Online Model Checker (ROMC) (Widlowski et al. 2007a) that was designed to find consistency among existing radiave transfer models through the developed and analysis of benchmark data sets. The models performance was evaluated against four heterogeneous baseline scenarios: HET01_DIS_UNI_RED and HET01_DIS_UNI_NIR and using zenith angles of 20 and 50 degrees. For all scenes, the fraction of absorptance by foliage elements (*fabs*) and the fractions of radiation impinging on the background surface (*ftran*) were computed from a number of photons varying between 4 and 10 million per scene. All *fabs* simulations showed consistency with the ROMC-Reference to within ~1%. Differences with the ROMC baseline for *ftran* were observed for the Near-Infrared case and the simulations showed a constant bias of around 4%.

A.2.2.2. deriving gap/hit probability

The ray tracer can be used to derive gap and hit probabilities from scenes that have materials specified with certain gap fractions, i.e. the degree of porosity of a surface when observed orthogonally. Individual elements that are intersected by a ray are ordered with respect to their distance from the ray's source and a hit probability is computed at every intersection based on the cosine angle with the element. At every intersection, in sorted order, the transmitted portion of the ray is computed as $I_i \cdot (1 - P_{hit})$, where I_i is the remaining payload after the previous intersection and I_0 is the payload of the primary ray, so that values I_0 of all primary rays originating from a hemisphere of light sources are equal and sum to one.

Table 1: Definition of parameters and symbols used in processing laser scanning data and the simulation of radiation transmission. Where applicable, parameter values are stated in italics.

F_{dist}, $F_{dist,ind}$	distance transformation, indices of nearest feature pixels
d	cumulative Manhattan distance
p_{MAT}	medial axis pixel (medial atom)
p_{left} , p_{right}	boundary pixels left and right of the medial axis
k	number of medial axis pixels
D	stem diameter
R	range
α_{span}	angular width of objects in the panoramically projected EVI data
$\delta_{i,j}$	range tolerance between neighbouring pixels *i* and *j* applicable to hard-targets *(0.3m)*
r	correlation coefficient (filtering criterion for stem detection) *(0.95)*
ξ	change in angle along the medial axis *(15°)*
n	the minimum number of pixels contained in a medial axis *(24)*
G	grid cell size of surface model *(0.4m)*
K	size of Gaussian smoothing kernel *(1.5m)*
σ_K	standard deviation of Gaussian smoothing kernel *(1m)*
m	PHM threshold distance for voting 'True' *(0.1m)*
Δz_l - Δz_u	parameter boundaries for z-displacement relative to local maximum *(-1 to 2m)*
$\alpha_l – \alpha_u$	parameter boundaries for cone opening angle *(10 to 24°)*
L	length of occlusion measured along the stem
w	connecting segment, used in bridging occlusion along stems
L_Z, $L_{Z,MAX}$	z-component of *L*, user defined maximum for L_Z *(10m)*
s, s_{MAX}	angle between paired tangent vectors, user defined maximum for *s* *(10°)*
$g(\vartheta_i)$	directional gap fraction of a branch *(0.15 at normal angle)*

Table 2: Comparison of terminology and variables typically used in forest mensuration and ecology vs. related parameters used in architectural tree models

forest mensuration/ecology	architectural tree models
clumping factor	distributions of 1st, 2nd and 3rd order branches
leaf area	number of leaves per branch
foliage profile	crown shape
diameter derived from pipe model	ratio branch width to length or branch order

Table 3: Sensitivity analysis of parameters *δ*, *r*, and *n* on percentage of correctly detected stems, and errors of commission and omission. Values for either *δ*, *n*, or *r* were changed while remaining parameters were kept constant. Constants used for sensitivity analysis were *δ*=0.3m, *n*=12, *r*=0.95.

***δ* (m)**	**0.1**	**0.2**	**0.3**	**0.4**	**0.5**	**trend**
Correctly detected	73.97%	82.53%	82.88%	83.90%	83.90%	+
Errors of commission	19.52%	14.73%	14.73%	12.67%	8.90%	-
Errors of omission	26.03%	17.47%	17.12%	16.10%	16.10%	-
n	**6**	**12**	**24**	**36**	**42**	
Correctly detected	89.73%	81.85%	75.34%	66.78%	64.04%	-
Errors of commission	61.30%	16.10%	0.34%	0.00%	0.00%	-
Errors of omission	10.27%	18.15%	24.66%	33.22%	35.96%	+
r	**0.7**	**0.8**	**0.9**	**0.99**	**0.995**	
Correctly detected	82.88%	82.88%	82.88%	82.88%	82.88%	0
Errors of commission	32.53%	32.19%	25.68%	15.41%	2.74%	-
Errors of omission	17.12%	17.12%	17.12%	17.12%	17.12%	0

Table 4: Parameter values used in the Arbaro architectural tree modeling software

level 0 trunk	**Value***	**Level 1 branches**	**Value***	**Level 2 branches**	**Value***
Shape	conical (n/a)	1DownAngle	90° (16%)	2DownAngle	45 ° **
levels	3 (n/a)	1DownAngleV	-50 (8%)	2Rotate	-90° (3%)
BaseSize	0.4 (30%)	1Rotate	140° **	2CurveRes	5 **
AttractionUp	-0.1 **	1CurveRes	25 (1%)		
		1Curve	-40° (2%)		

* Parameter sensitivity is shown between parenthesis and is expressed as the difference in cumulative hit distribution (x100%) caused by a +20% and -20% change of the listed parameter value. Sensitivities were computed for one parameter at a time, while remaining model parameters were kept constant.

** Parameters for which sensitivity was less than 1%.

Figures

Figure 1: Schematic representation of the stem detection algorithm showing the individual steps of processing. See text for explanations about the individual processing steps.

Figure 2: A schematic of the complete processing pipeline used for reconstructing plots.

Figure 3: Binary image showing clusters of pixels with 8-connected neighbors within range, *δ (a)*. Distance transformation and projection of the Medial Axis Transformation overlaid in red (b). Stem detection overlaid on laser intensity image (c).

Figure 4: Detection rate as a function of radial distance from the scanner's location.

Figure 5: Linear regression of EVI derived-, and tape measured diameter at breast height indicates an underestimation of diameters derived from EVI data.

Figure 6: Co-registration of TLS stem locations for the north-east (blue), south-east (purple), north-west (yellow), south-west (magenta) and centre (red) locations within the plot, against field measured stem locations (green) for plot 2. Diameter estimates are indicated by the size of the markers. Trees that were detected in the TLS scans and for which no DBH information was derived as a result of occlusion around breast height are shown in their respective scan colours as plus-signs (+).

Figure 7: 3D map of stem reconstructions (a). Detail of one reconstructed tree and its neighboring point cloud (b). (The neighboring tree visible in the point cloud was also detected.)

Figure 8: Fitting of planar polygons to Arbaro branch models and scaling of crowns to the tree growing spaces.

Figure 9: Illustration of reconstructions for all four plots. Shown are the woody skeletons produced by Arbaro software and fitted to the tree growing spaces (a) and the fitting of planar polygons to simulate the layering of foliage elements in coniferous canopies (b).

Figure 10: Facet area profiles (bars) derived from mesh reconstructions and point cloud information and full waveform EVI derived leaf area profiles (solid black line) per square meter ground surface area for the four plot reconstructions.

Figure 11: Hit distributions for the four plot reconstructions and fitted trend lines. The profiles show an increase in the mid canopy and an increase near the forest floor, and considerable variation in absorption around the trend lines.

Figure 12: Cumulative hit distribution against EVI P_{gap} measured around different zenith angles.

Figure 13: Arbaro parameter sensitivity analysis. Variation induced by the six most important parameters is displayed along the diagonal of the matrix of plots, while effects of co-varying two parameters on the cumulative hit distribution is displayed in the upper half, and the observed range in model outcome in the lower half.

Figure 14: Effect of altering distributions for gap fraction $g(\vartheta_i)$ on the cumulative hit distribution for all four plots.

Figure 1.

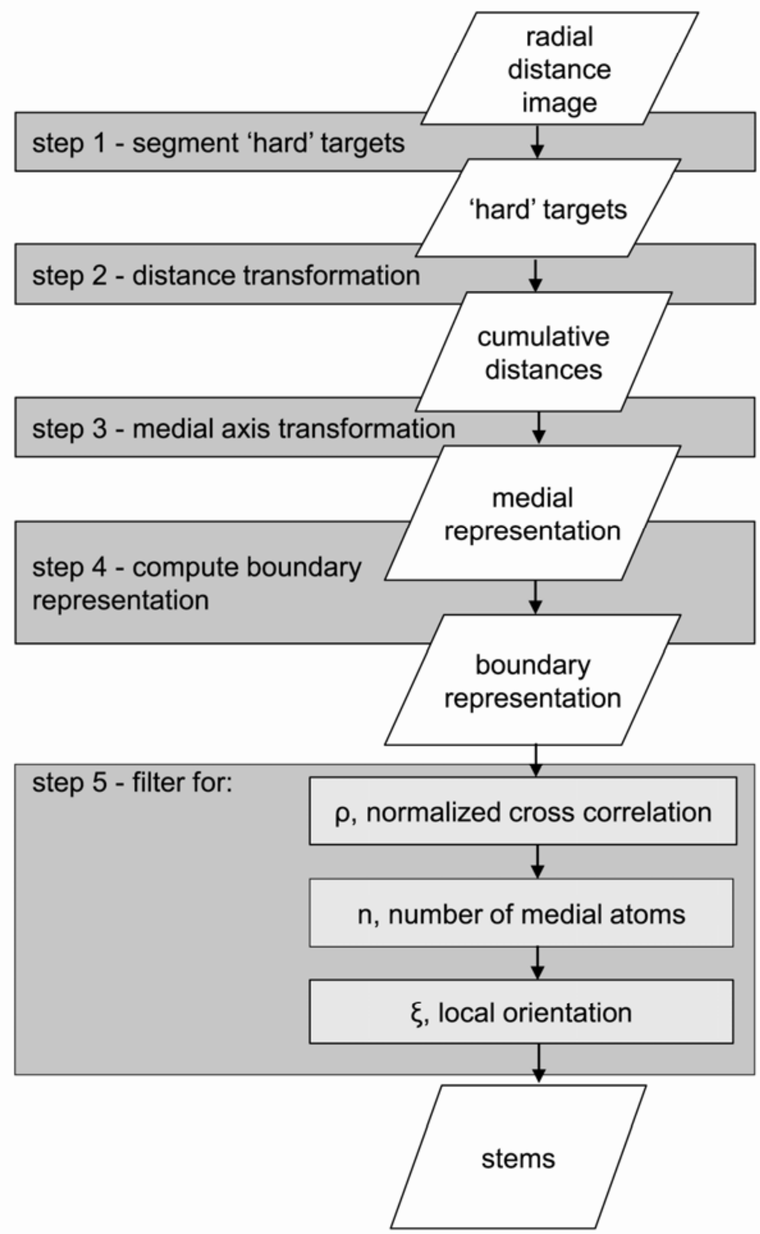
radial distance image
step 1 - segment 'hard' targets
'hard' targets
step 2 - distance transformation
cumulative distances
step 3 - medial axis transformation
medial representation
step 4 - compute boundary representation
boundary representation
step 5 - filter for:
ρ, normalized cross correlation
n, number of medial atoms
ξ, local orientation
stems

Figure 2.

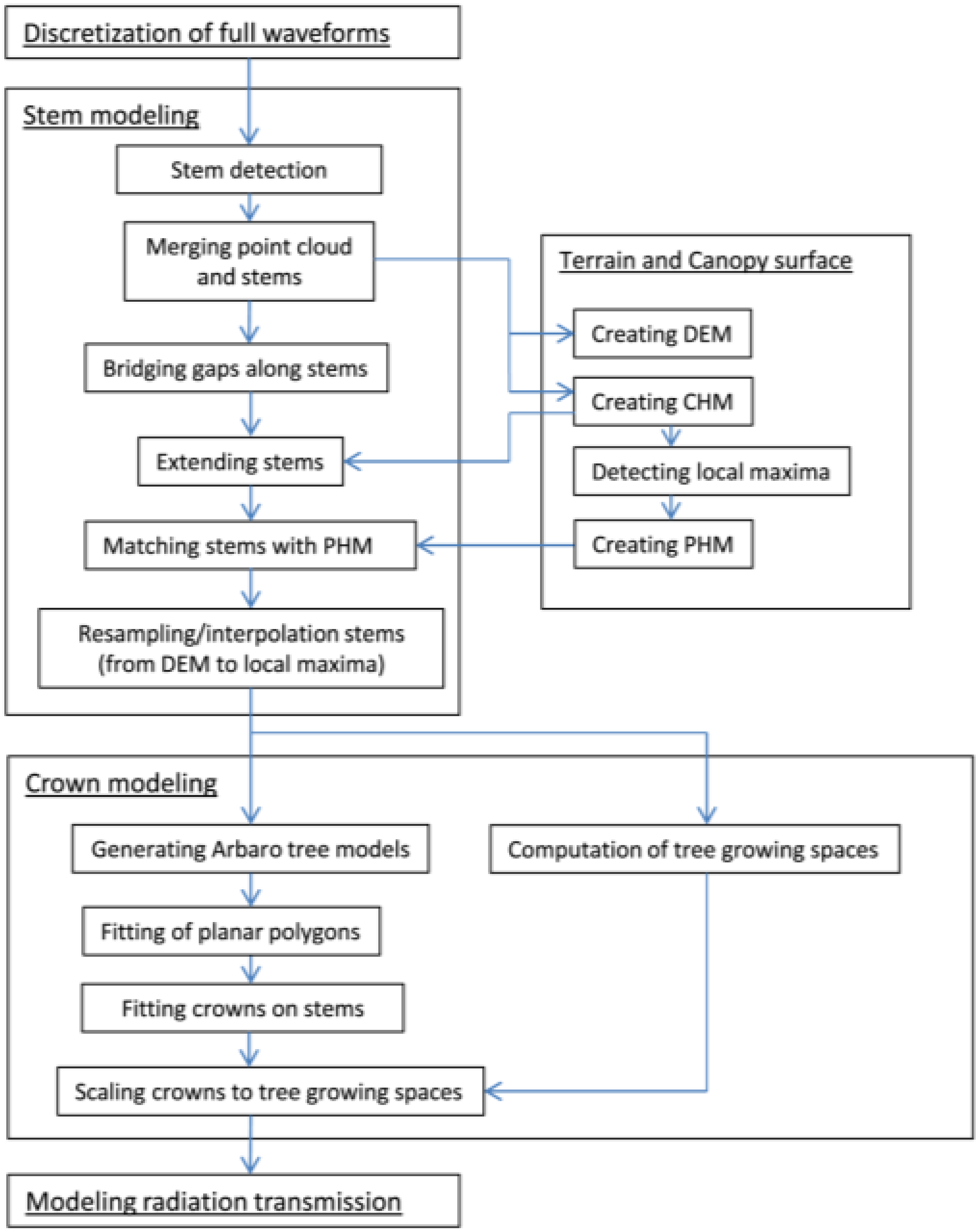

Discretization of full waveforms
Stem modeling
Stem detection
Merging point cloud and stems
Bridging gaps along stems
Extending stems
Matching stems with PHM
Resampling/interpolation stems (from DEM to local maxima)
Terrain and Canopy surface
Creating DEM
Creating CHM
Detecting local maxima
Creating PHM
Crown modeling
Generating Arbaro tree models
Computation of tree growing spaces
Fitting of planar polygons
Fitting crowns on stems
Scaling crowns to tree growing spaces
Modeling radiation transmission

Figure 3

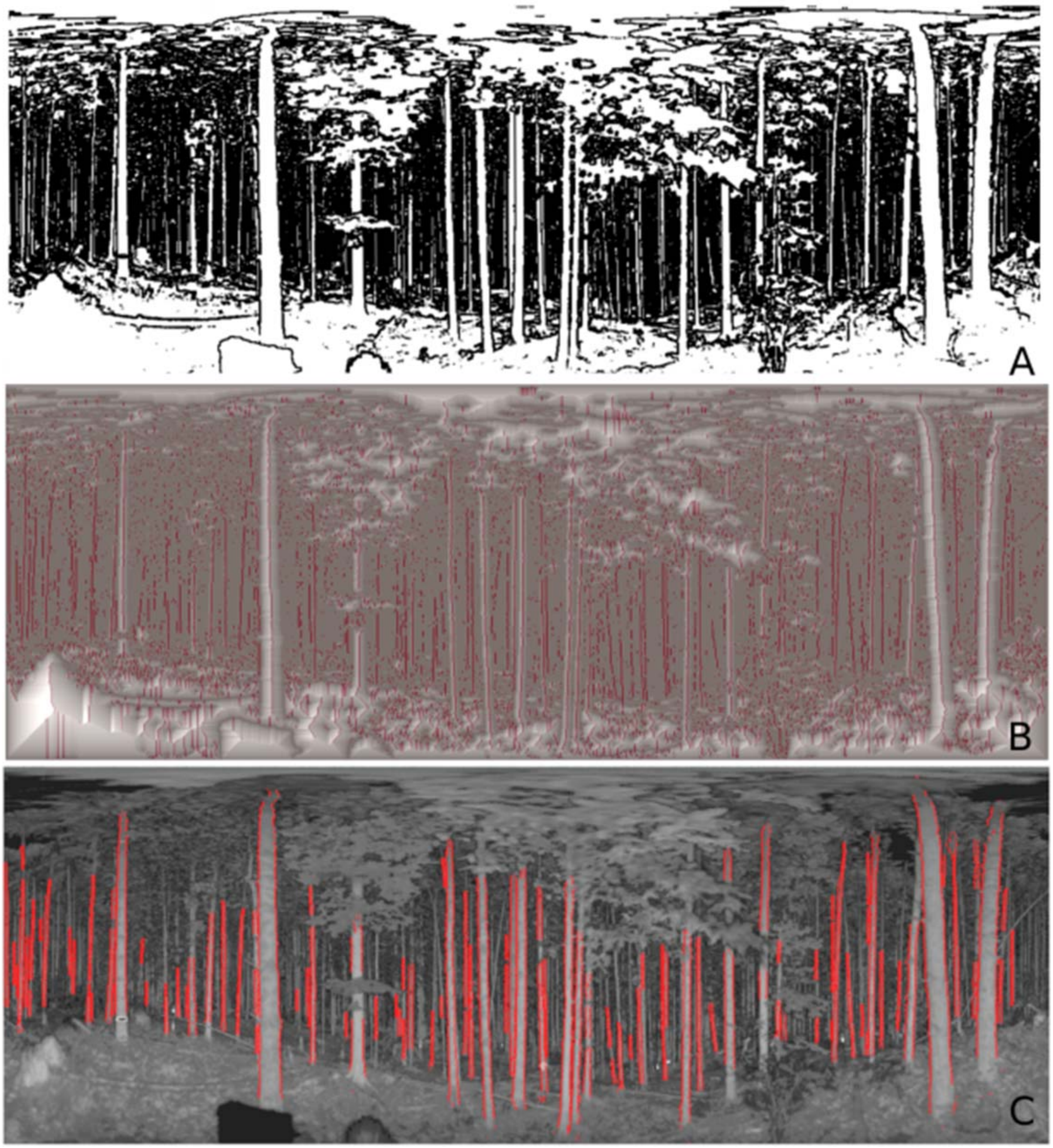

Figure 4

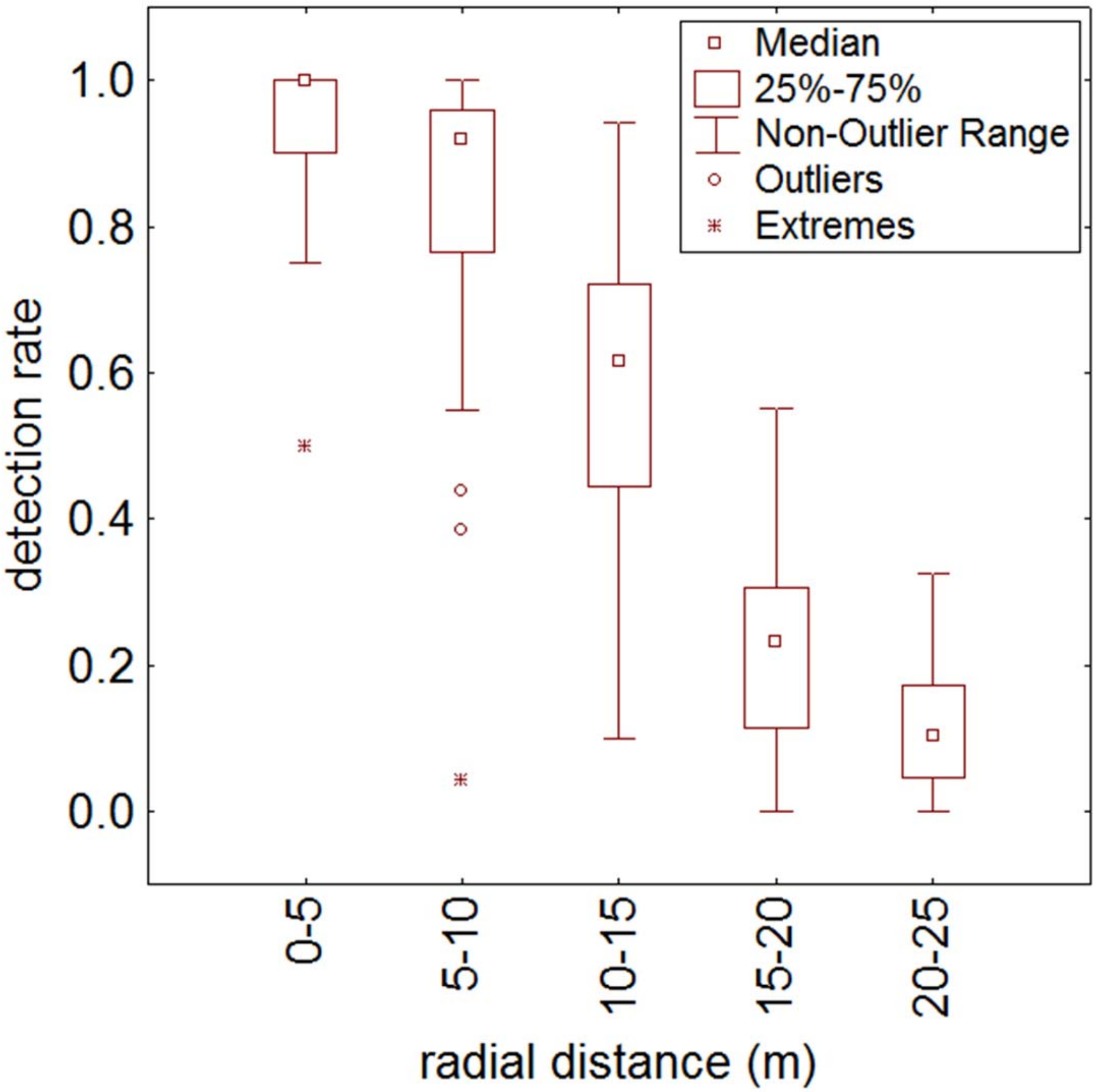

Median
25%-75%
Non-Outlier Range
Outliers
Extremes
1.0
0.8
0.6
0.4
0.2
0.0
detection rate
0-5
5-10
10-15
15-20
20-25
radial distance (m)

Figure 5

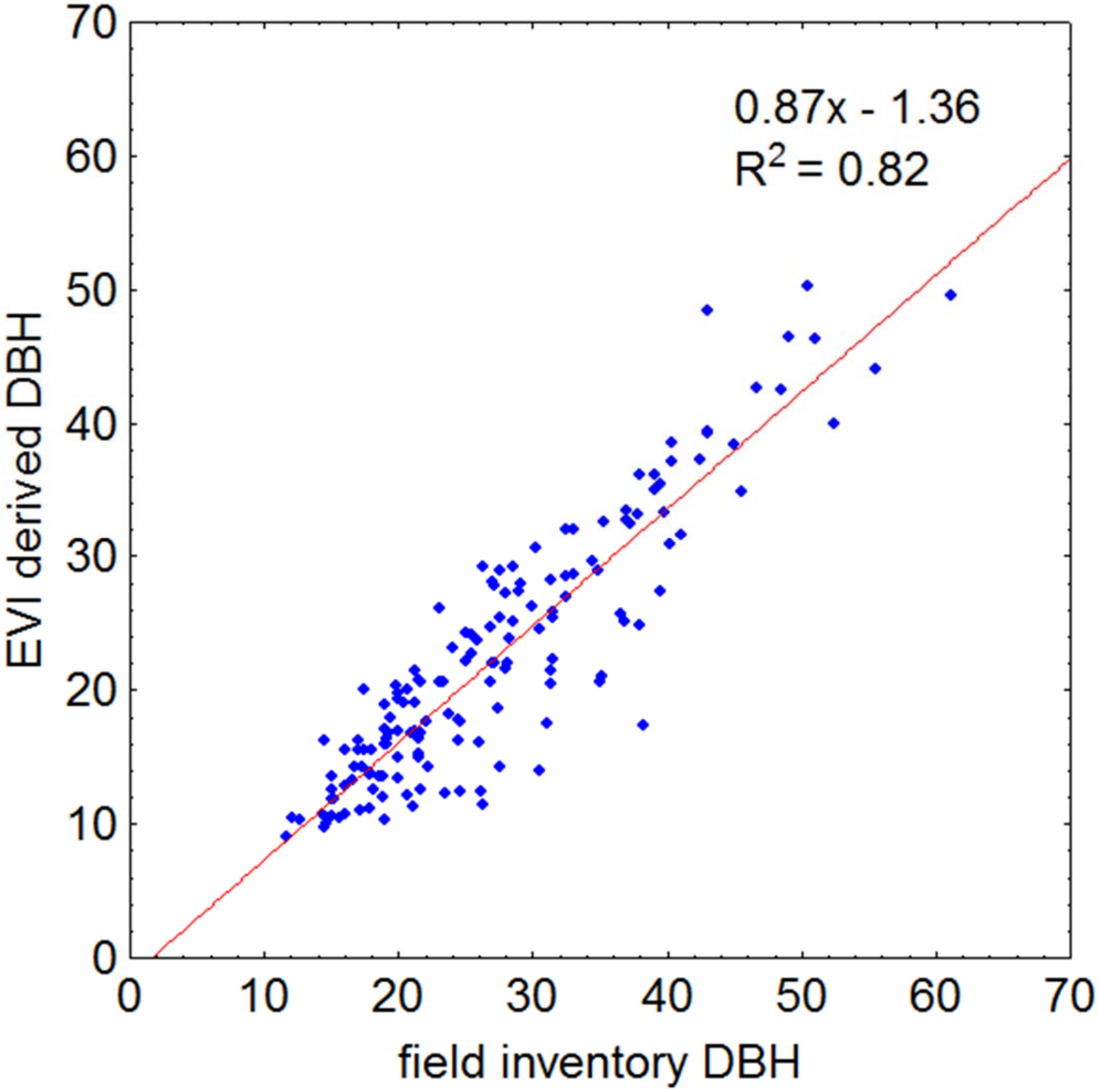

0.87x - 1.36
R^2 = 0.82
EVI derived DBH
field inventory DBH
0
10
20
30
40
50
60
70

Figure 6

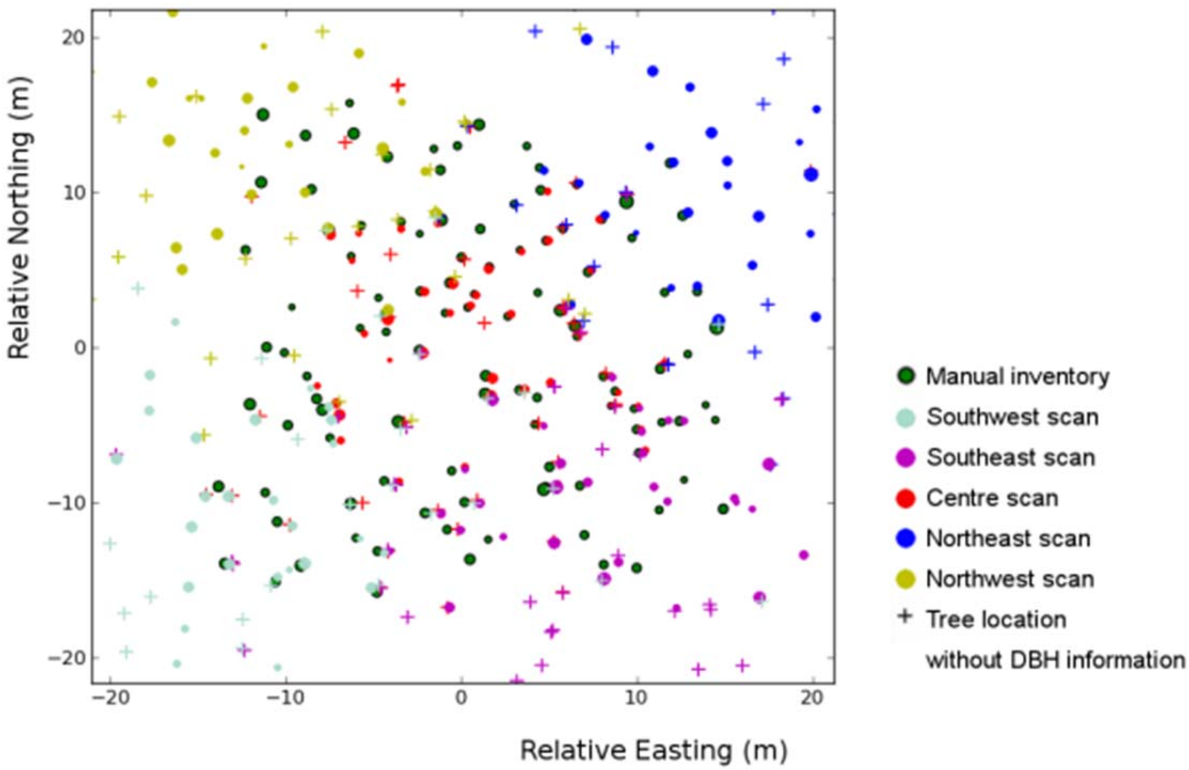
Relative Northing (m)
Relative Easting (m)
20
10
0
−10
−20
−20
−10
0
10
20
Manual inventory
Southwest scan
Southeast scan
Centre scan
Northeast scan
Northwest scan
Tree location
without DBH information

Figure 7

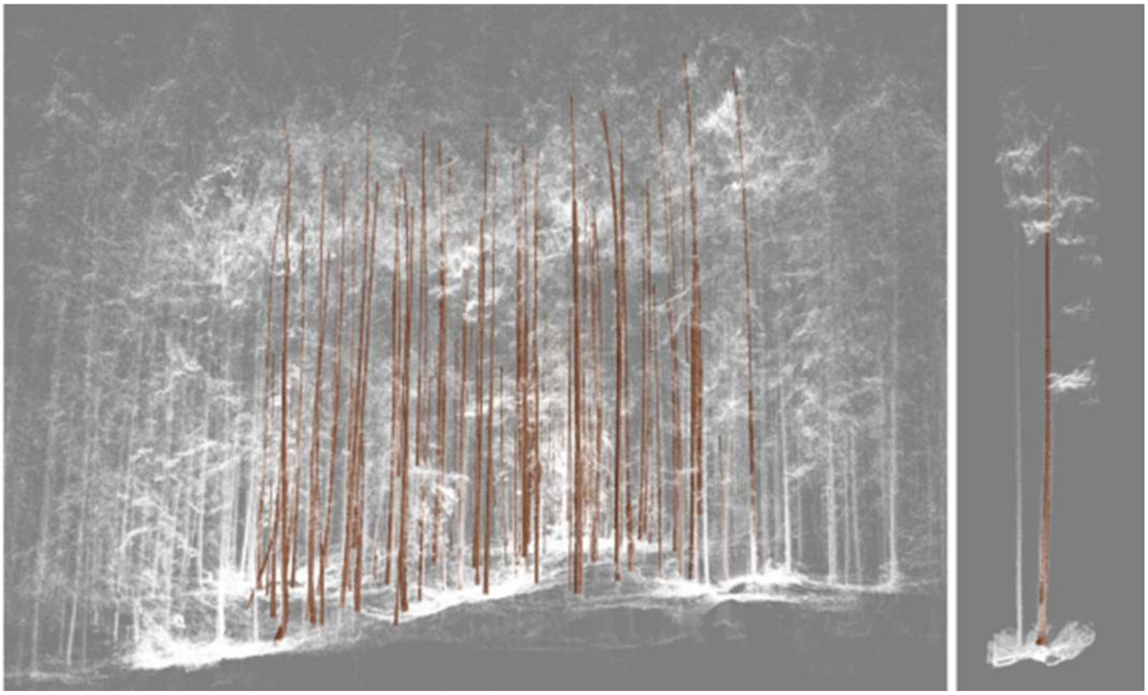

Figure 8

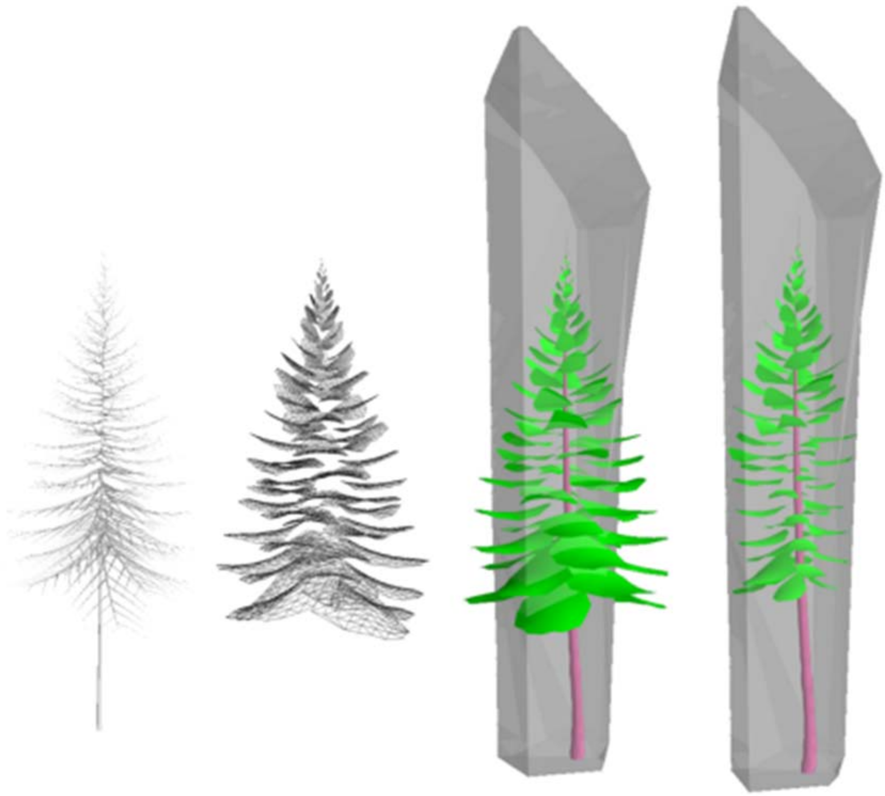

Figure 9

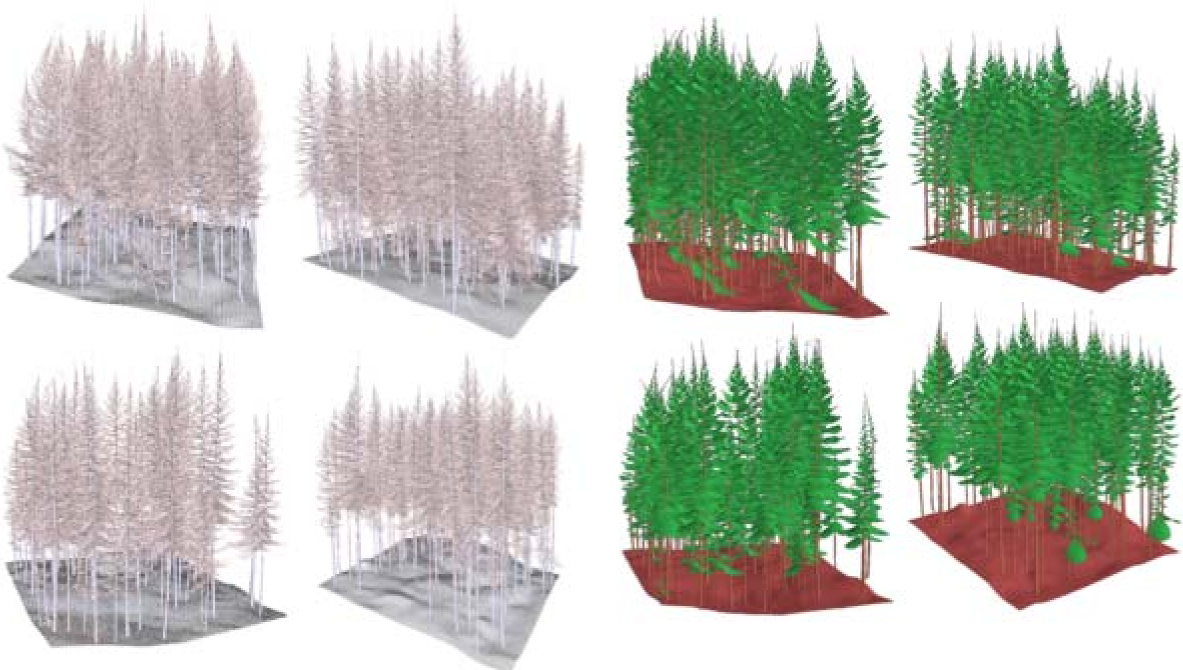

Figure 10

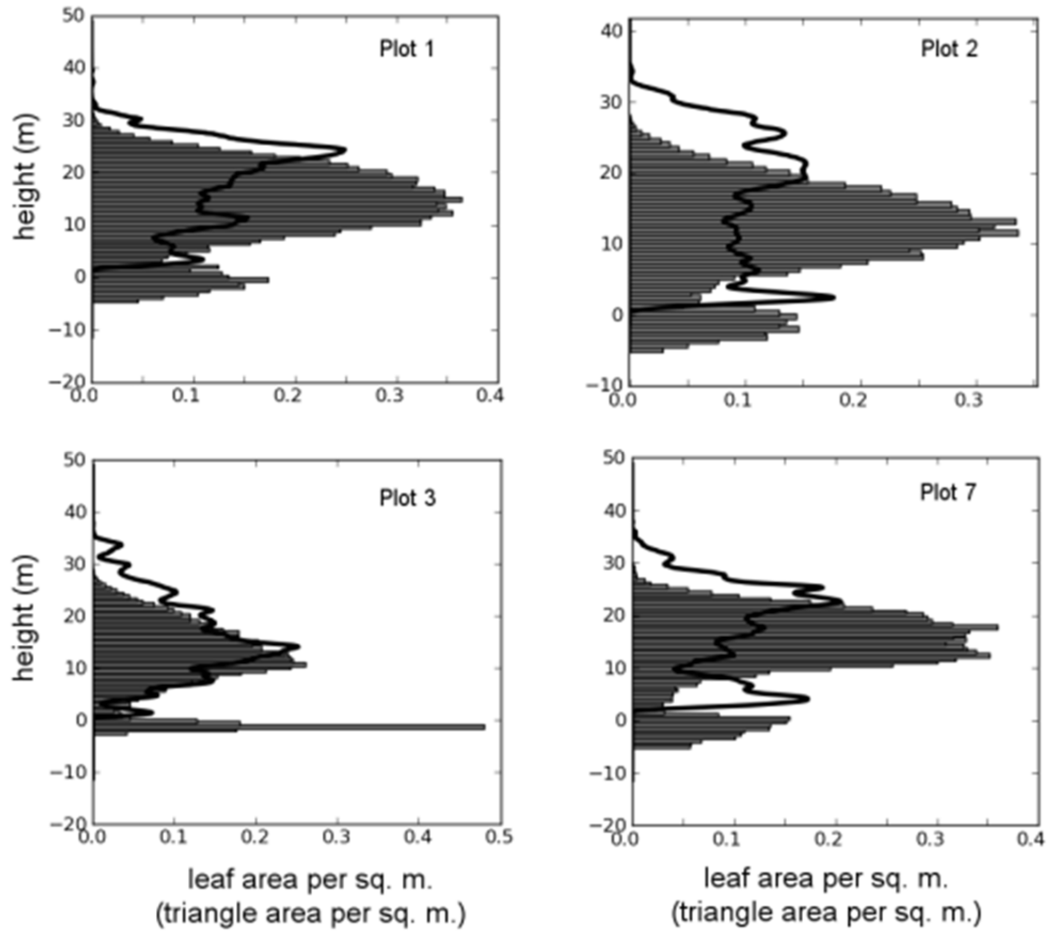

Plot 1
Plot 2
Plot 3
Plot 7
height (m)
height (m)
leaf area per sq. m.
(triangle area per sq. m.)
leaf area per sq. m.
(triangle area per sq. m.)

Figure 11

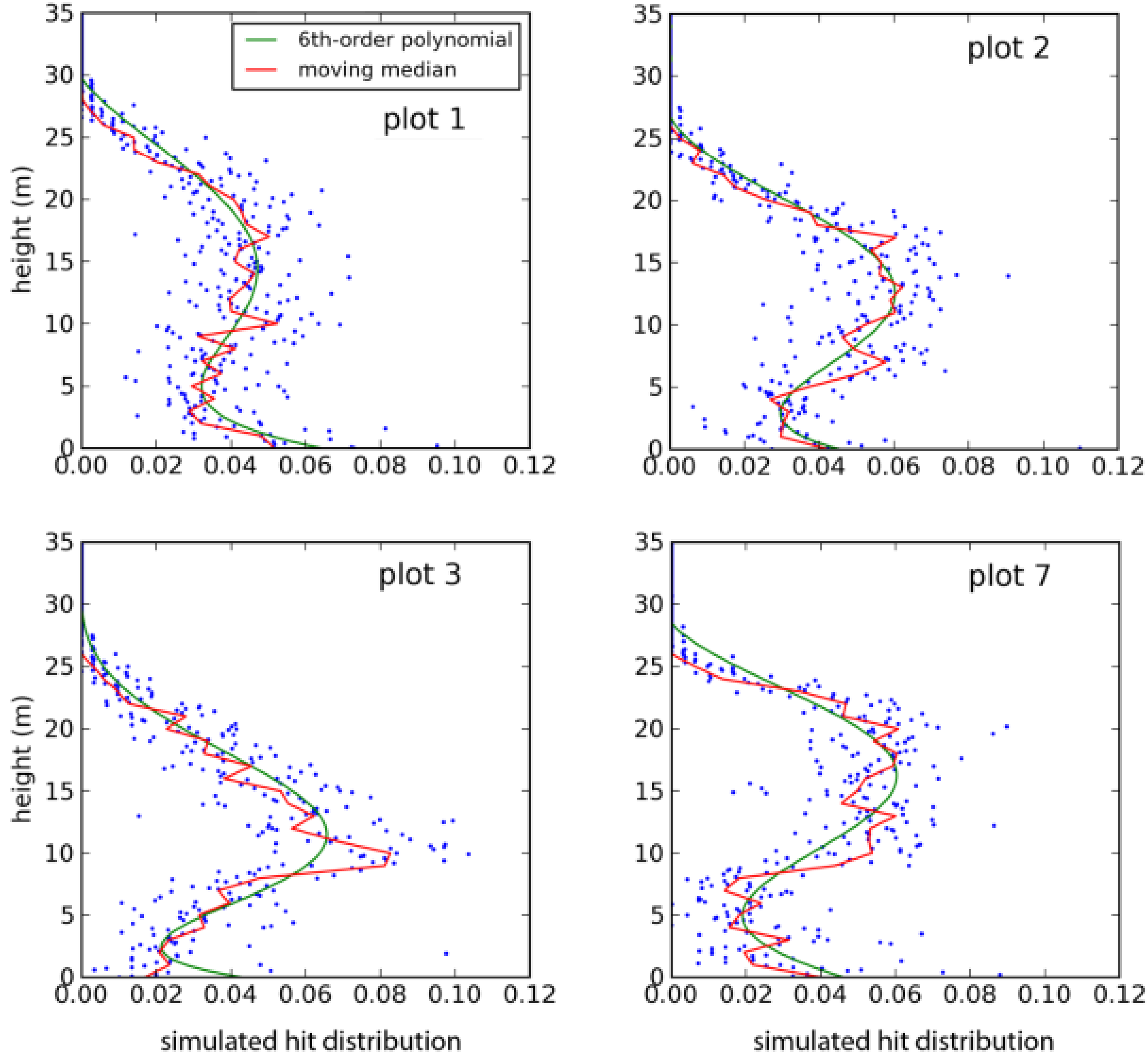
6th-order polynomial
moving median
plot 1
plot 2
plot 3
plot 7
height (m)
height (m)
simulated hit distribution
simulated hit distribution
0.00
0.02
0.04
0.06
0.08
0.10
0.12
0
5
10
15
20
25
30
35

Figure 12

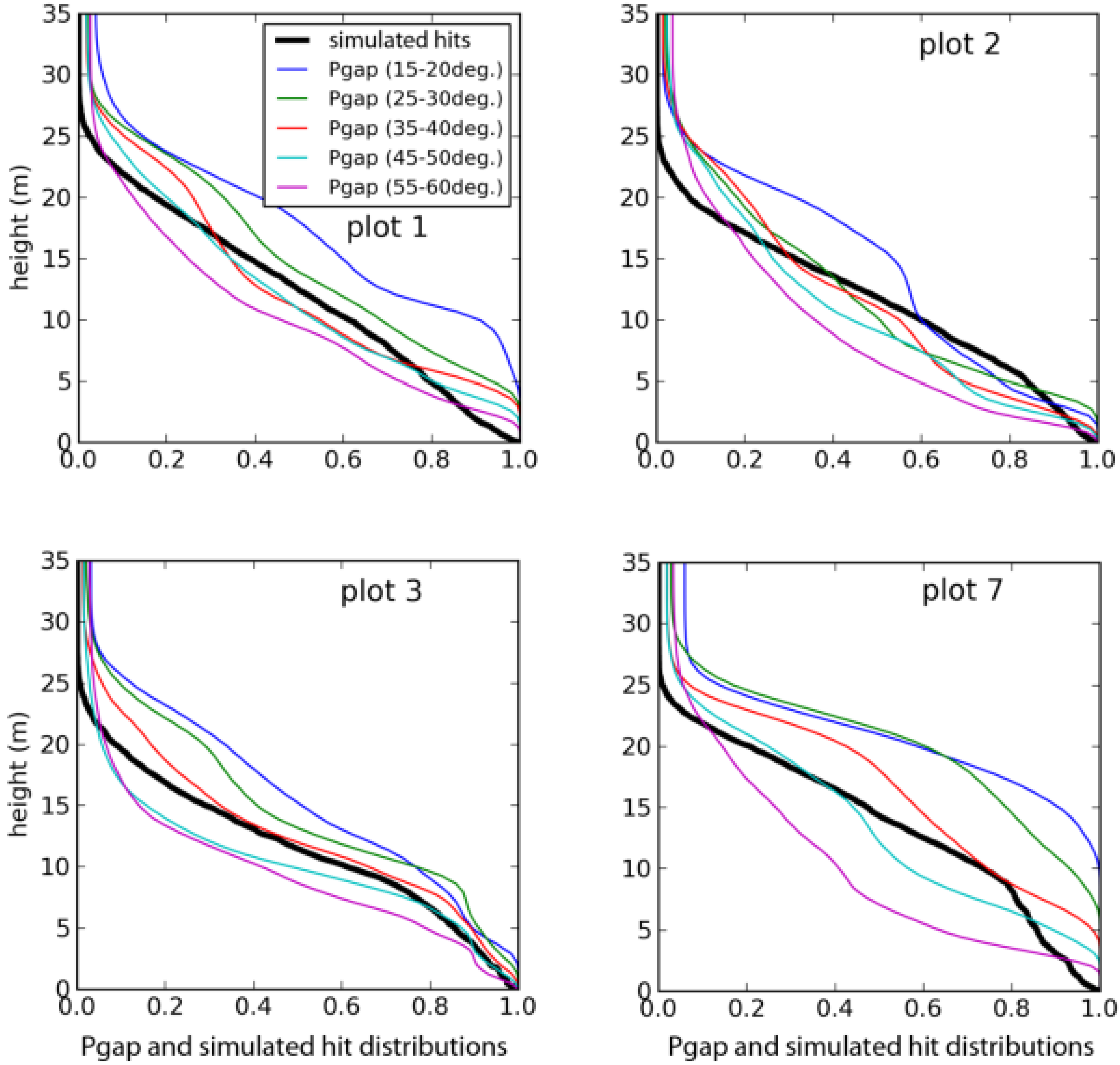
simulated hits
Pgap (15-20deg.)
Pgap (25-30deg.)
Pgap (35-40deg.)
Pgap (45-50deg.)
Pgap (55-60deg.)
plot 1
plot 2
plot 3
plot 7
height (m)
Pgap and simulated hit distributions
0
5
10
15
20
25
30
35
0.0
0.2
0.4
0.6
0.8
1.0

Figure 13

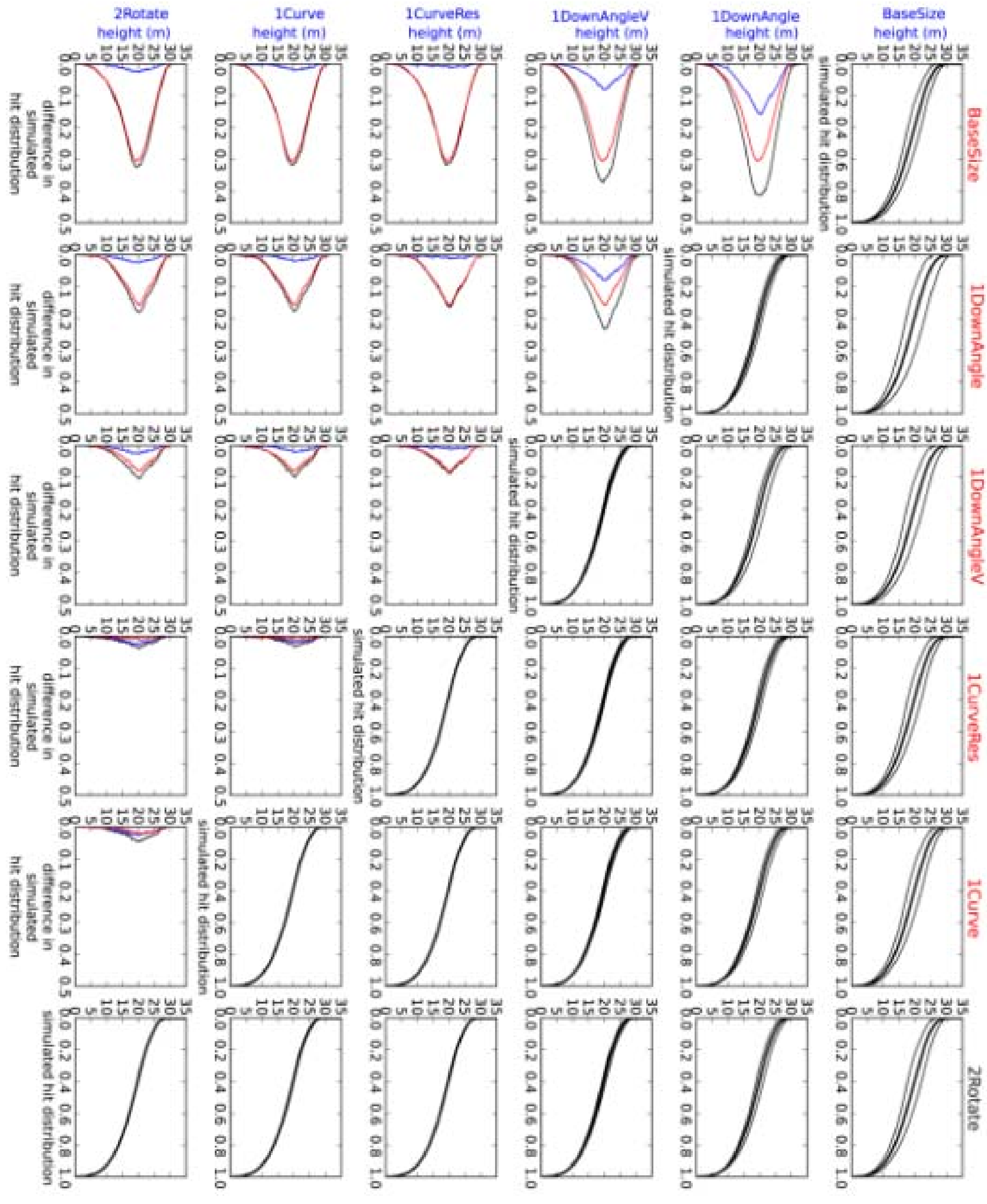
BaseSize
1DownAngle
1DownAngleV
1CurveRes
1Curve
2Rotate
height (m)
simulated hit distribution
difference in simulated hit distribution

Figure 14

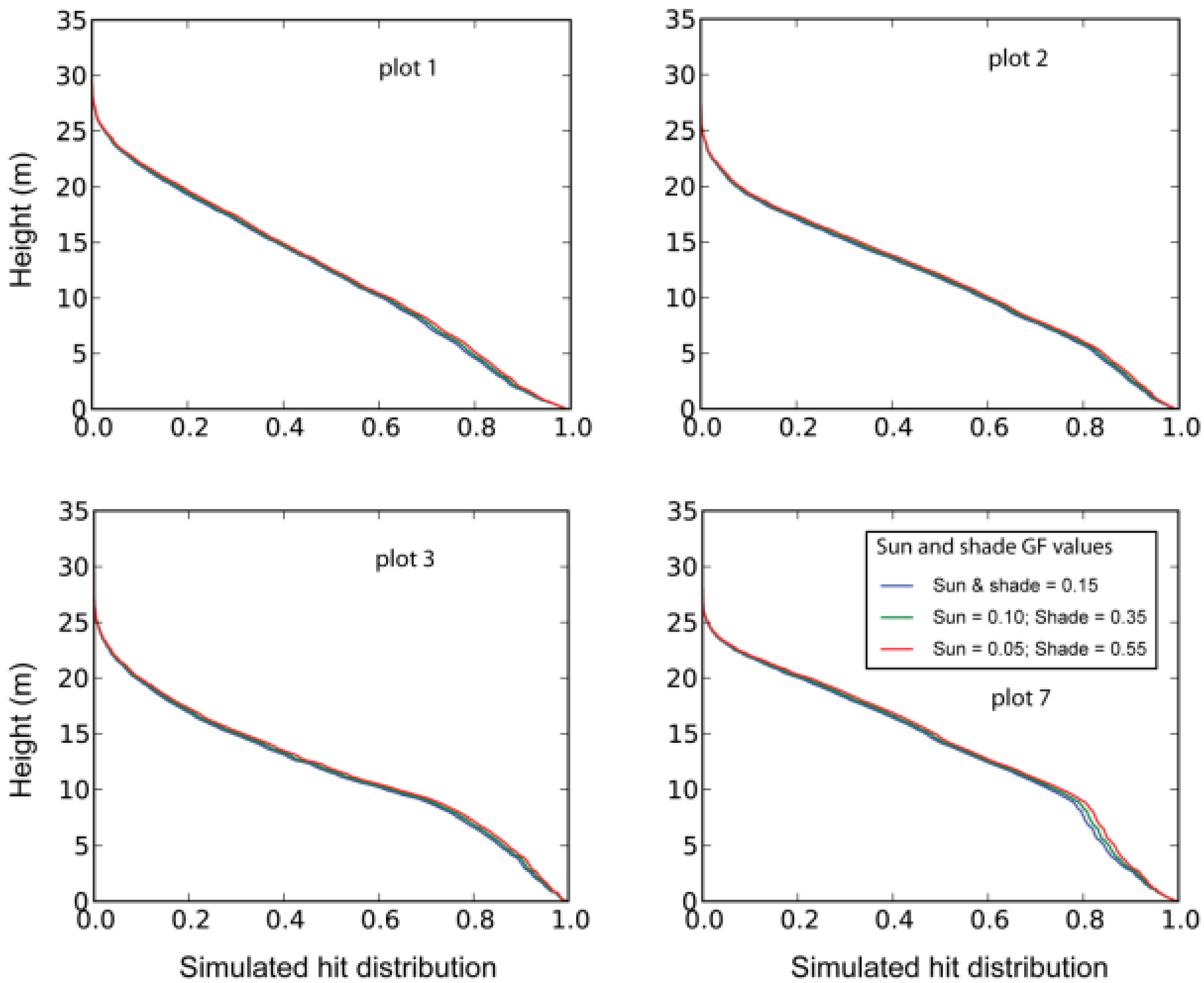
plot 1
plot 2
plot 3
plot 7
Height (m)
Simulated hit distribution
Sun and shade GF values
Sun & shade = 0.15
Sun = 0.10; Shade = 0.35
Sun = 0.05; Shade = 0.55